Misura di sin 2β

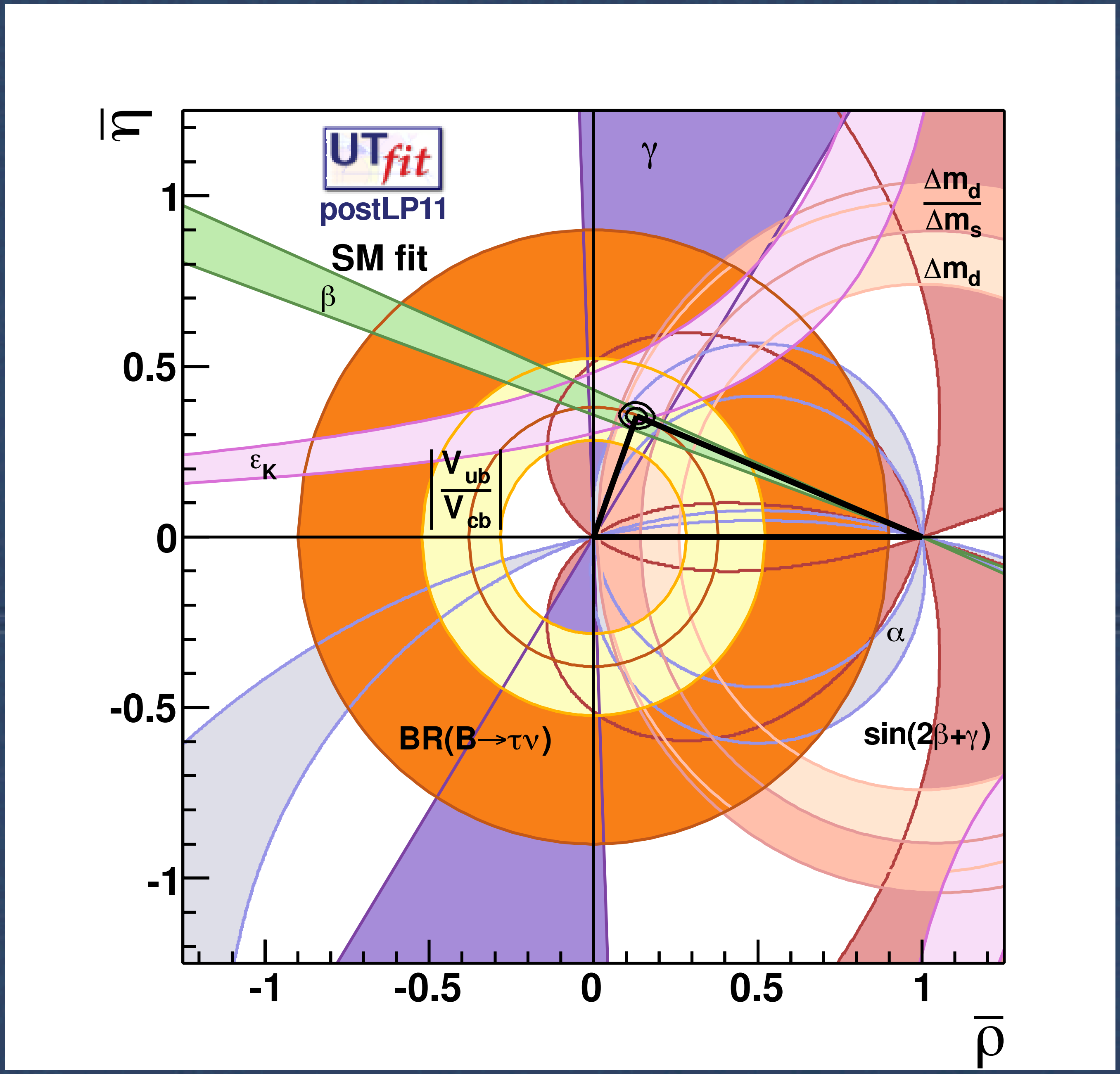

E.Paoloni (INFN & Università di Pisa)

BABAR Collaboration

Il Detector BaBar

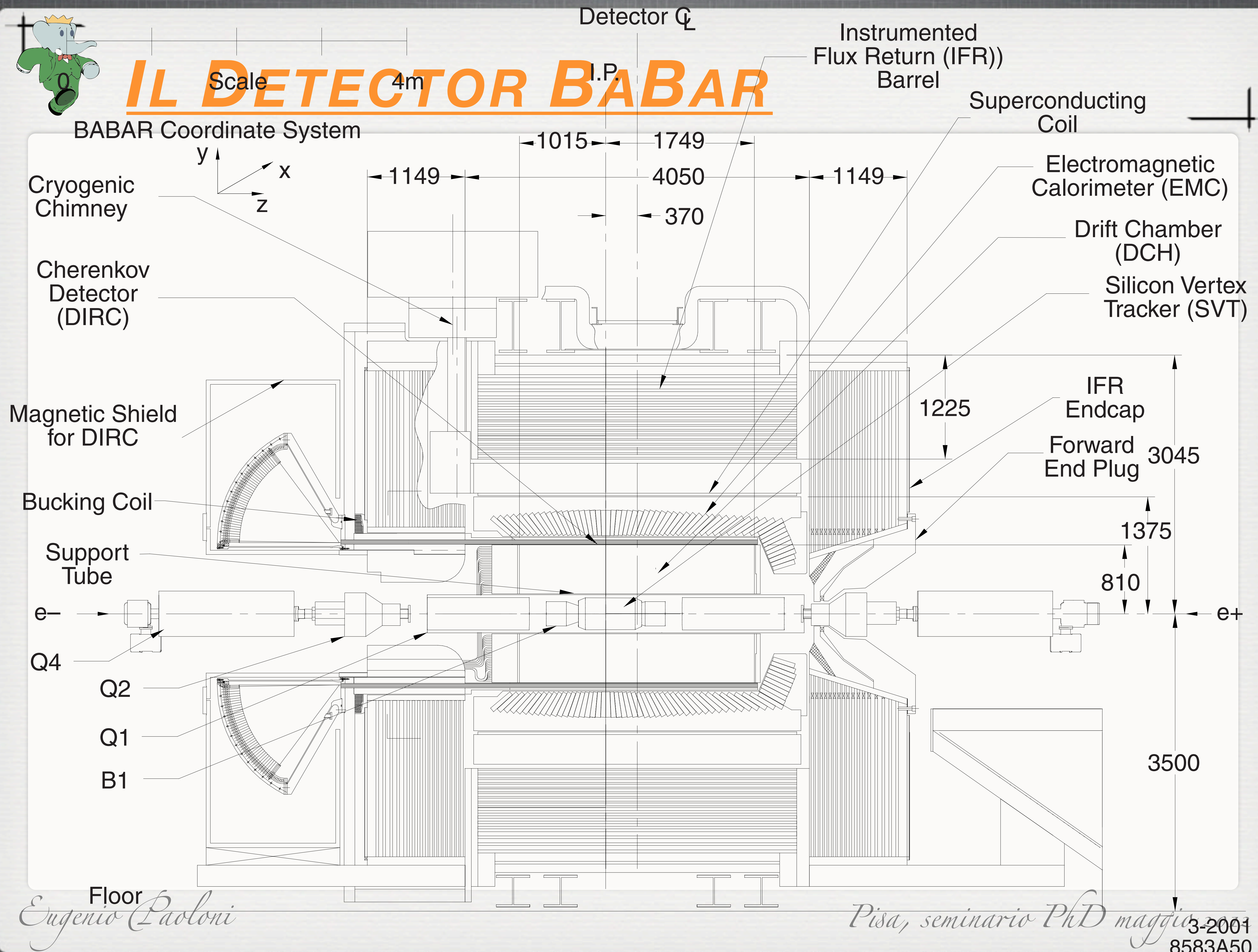

IL DETECTOR

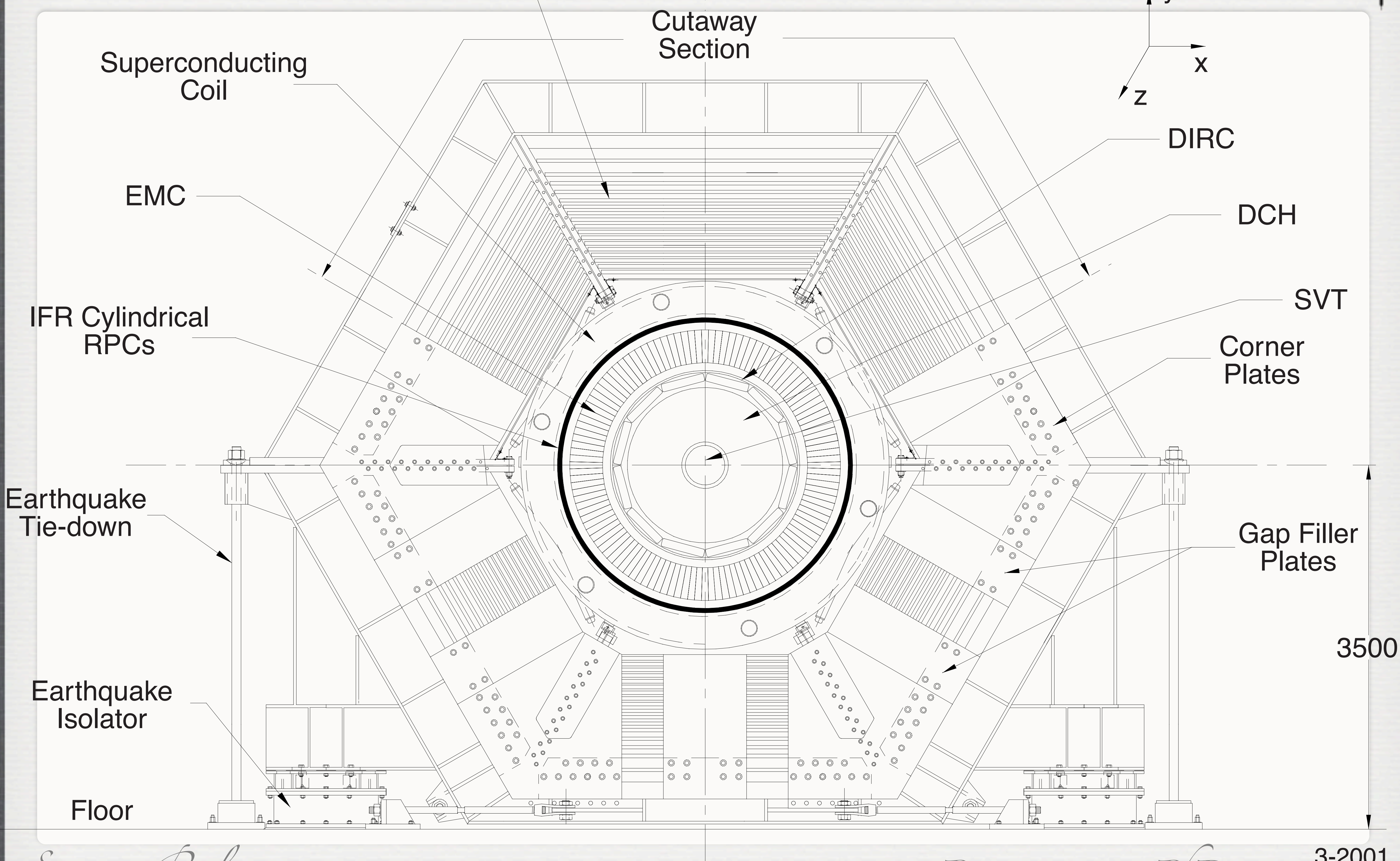
IFR Barrel
0
Scale
4m
BABAR Coordinate System
y
x
z
Cutaway
Section
Superconducting
Coil
DIRC
EMC
DCH
SVT
IFR Cylindrical
RPCs
Corner
Plates
Earthquake
Tie-down
Gap Filler
Plates
3500
Earthquake
Isolator
Floor
3-2001
8583A51

Solenoide

MAGNETIC SPECTROMETER

$$\frac{d\vec{p}}{dt} = q\,\vec{v} \times \vec{B}$$

$|\vec{v}|$ è costante quindi $dt = ds/|\vec{v}|$

$$|\vec{v}|\frac{d\vec{p}}{ds} = q\,\vec{v} \times \vec{B}$$

$$\frac{d\vec{p}}{ds} = q\,\hat{v} \times \vec{B}$$

se $\vec{B}$ è costante le traiettorie sono eliche.

$$\rho = \frac{|\vec{p_\perp}|}{q|\vec{B}|}\ \text{(S.I.)}$$

$$\rho = \frac{|\vec{p_\perp}|}{0.29979 \cdot Z|\vec{B}|}$$

(p in GeV/c, B in T, ρ in m)

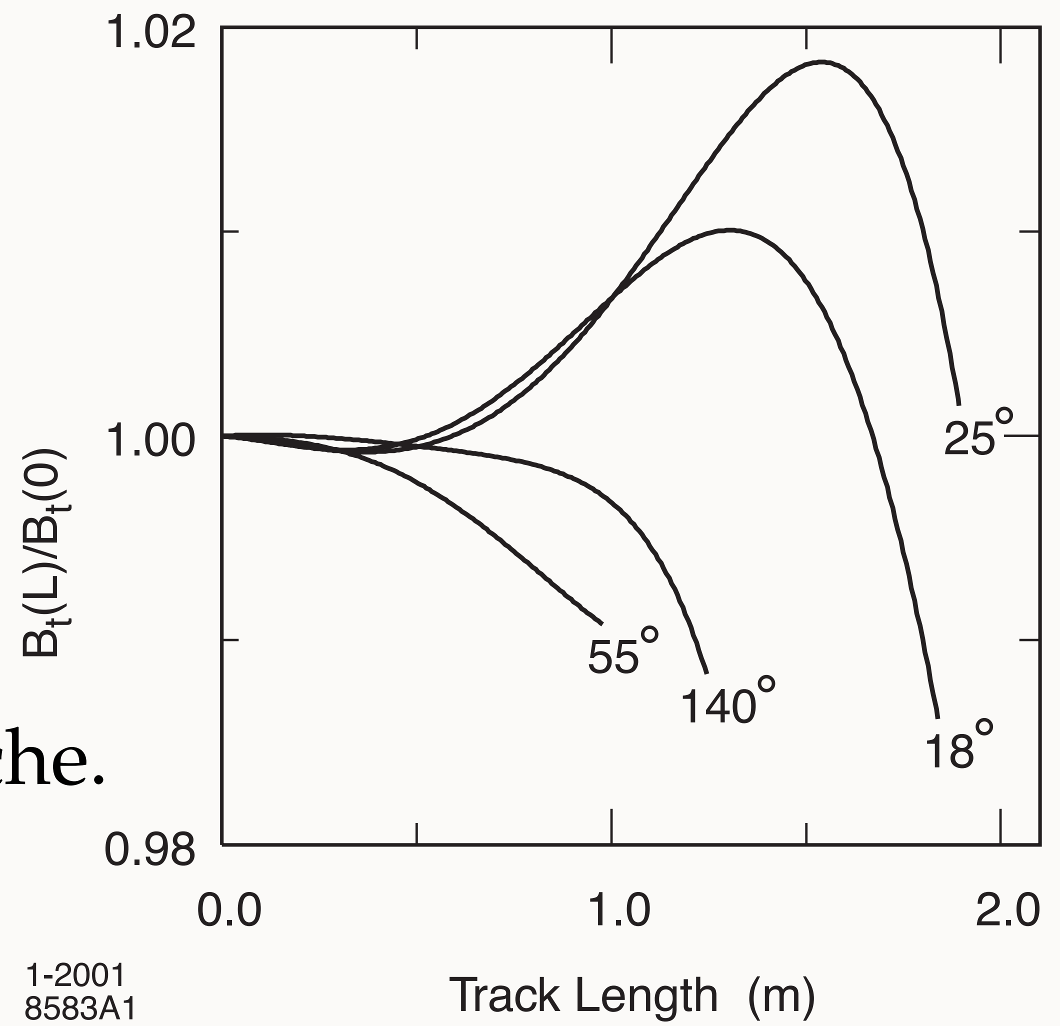

Figure 15. Relative magnitude of magnetic field transverse to a high momentum track as a function of track length from the IP for various polar angles (in degrees). The data are normalized to the field at the origin.

PARAMETERS

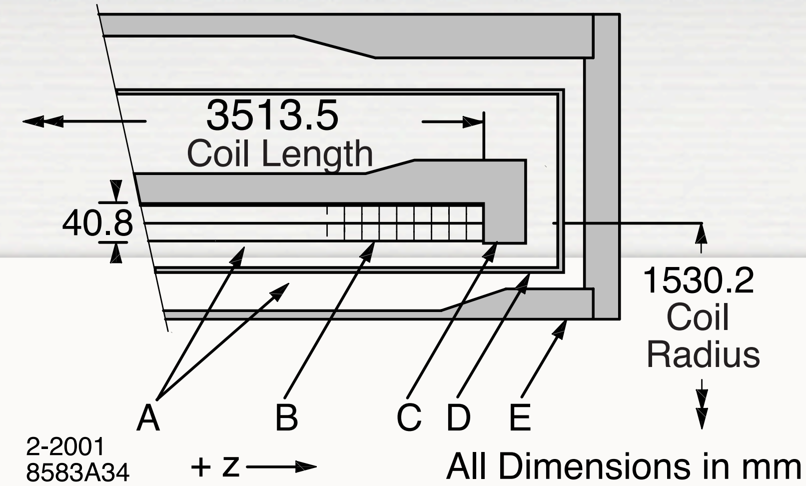

Figure 13. A portion of cryostat assembly. The forward end is shown. Legend: (A) evacuated spaces filled with IR-reflective insulator; (B) superconducting coil (2-layers); (C) aluminum support cylinder; (D) aluminum heat shield; (E) aluminum cryostat housing.

Magnet Parameters

Field Parameters		
Central Field	1.5	T
Max. Radial Field at Q1 and $r = 200\,\mathrm{mm}$	<0.25	T
Leakage into PEP-II	<0.01	T
Stored Energy	27	MJ
Main Coil Parameters		
Mean Diameter of Current Sheet	3060	mm
Current Sheet Length	3513	mm
Number of layers	2	
Operating Current	4596	A
Conductor Current Density	1.2	$\mathrm{kA/mm^2}$
Inductance	2.57	H

27 MJ ~ 20 Tonnellate @ 180 km/h

Silicon Vertex Tracker

Rivelatore di Vertice

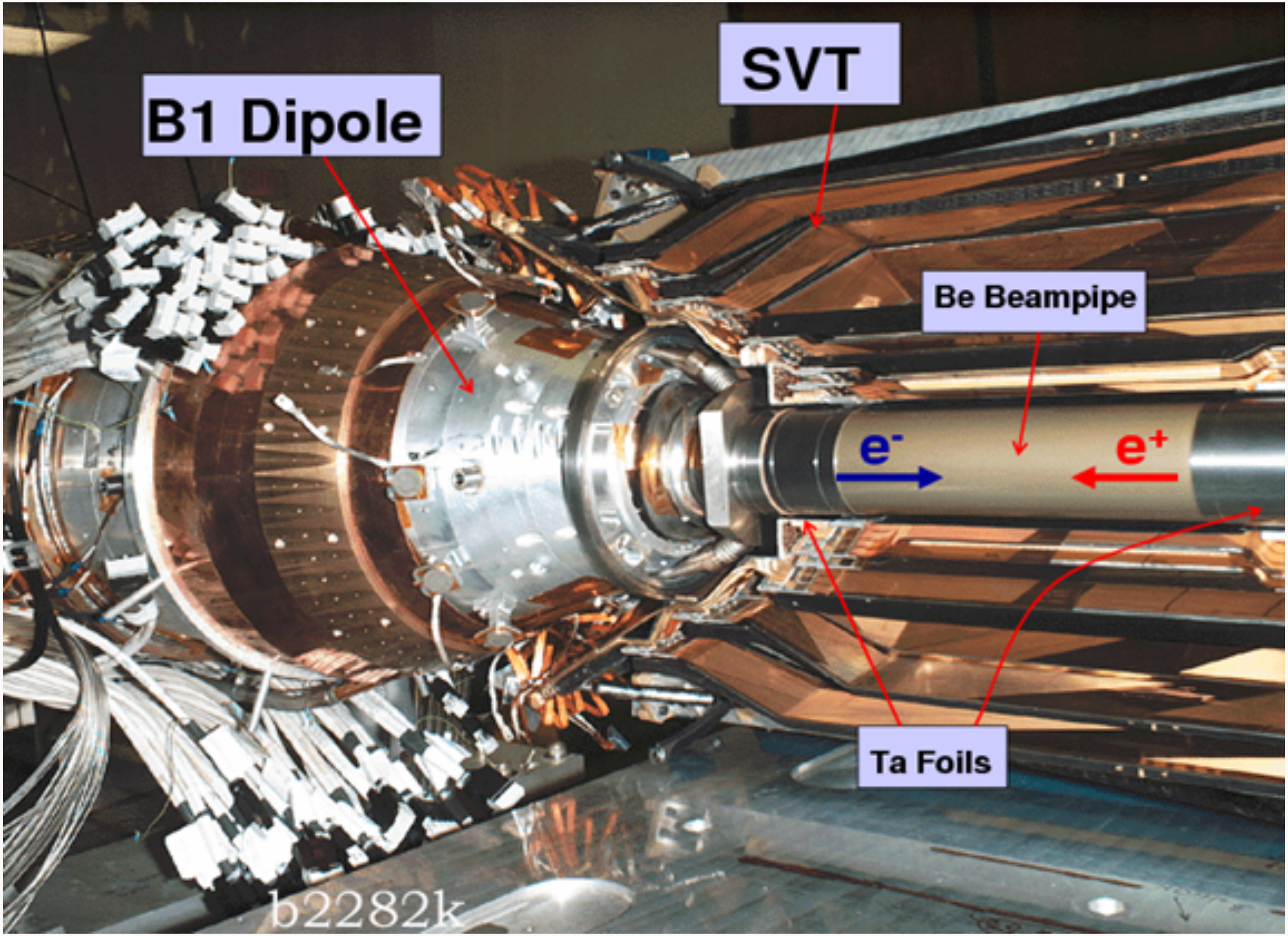

SVT Caratteristiche Meccaniche

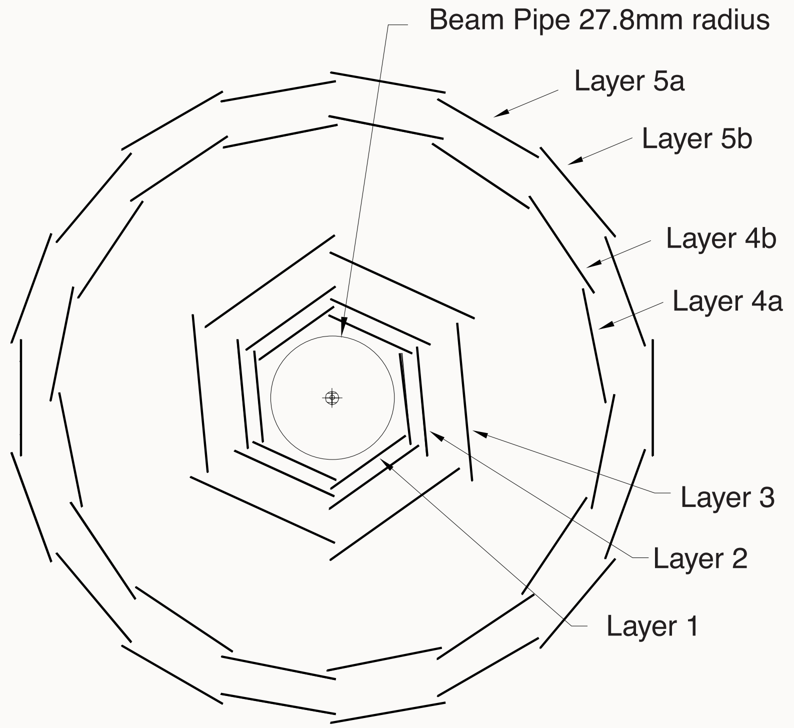

Layer/ view	Radius (mm)	R-O pitch (μm)	Floating strips	Strip length (mm)
1 z	32	100	1	40
1 ϕ	32	50-100	0-1	82
2 z	40	100	1	48
2 ϕ	40	55-110	0-1	88
3 z	54	100	1	70
3 ϕ	54	110	1	128
4 z	91-127	210	1	104
4 ϕ	91-127	100	1	224
5 z	114-144	210	1	104
5 ϕ	114-144	100	1	265

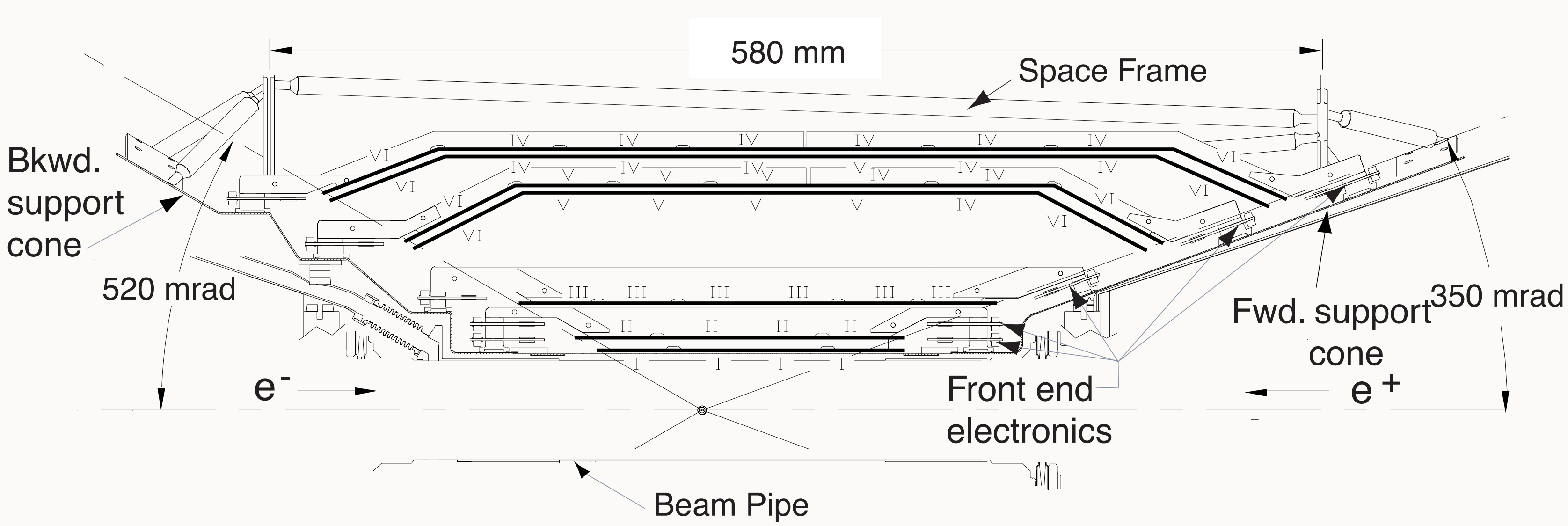

Figure 17. Schematic view of SVT: longitudinal section. The roman numerals label the six different types of sensors.

Figure 19. Photograph of an SVT arch module in an assembly jig.

READOUT CHIP

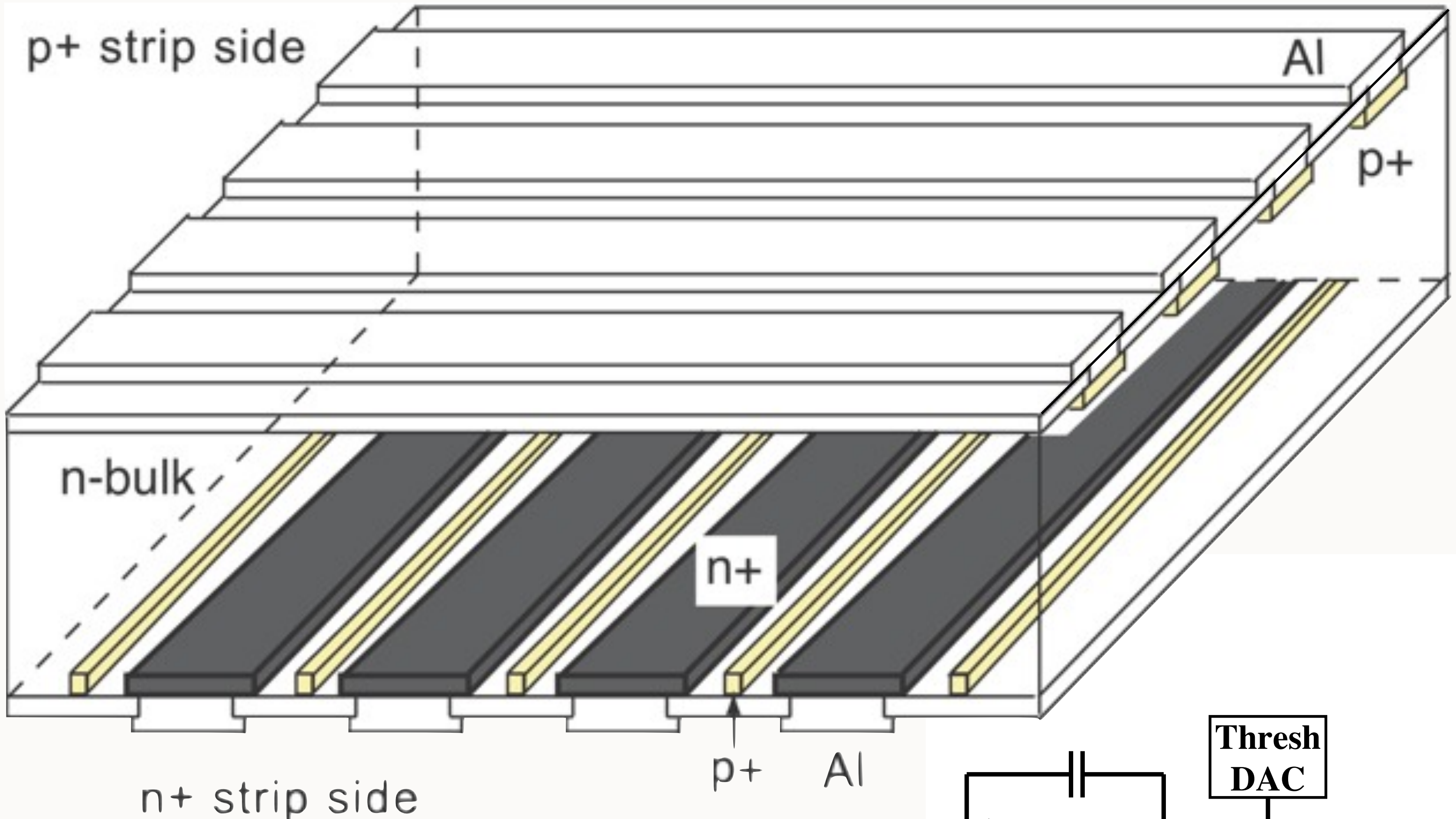

Layer/ view	C_{input} (pF)	R_{series} (Ω)	Noise, calc. (elec)	meas. (elec)
1 z	6.0	40.	550	880
1 ϕ	17.2	164.	990	1200
2 z	7.2	48.	600	970
2 ϕ	18.4	158.	1030	1240
3 z	10.5	70.	700	1180
3 ϕ	26.8	230.	1470	1440
4 z	16.6	104.	870	1210
4 ϕ	33.6	224.	1380	1350
5 z	16.6	104.	870	1200
5 ϕ	39.7	265.	1580	1600

Table 7
ATOM chip ENC parameters at different peaking times

Peaking time	ENC (0 pF)	Noise slope
100 ns	380 e^-	40.9 e^-/pF
200 ns	280 e^-	33.9 e^-/pF
400 ns	220 e^-	25.4e^-/pF

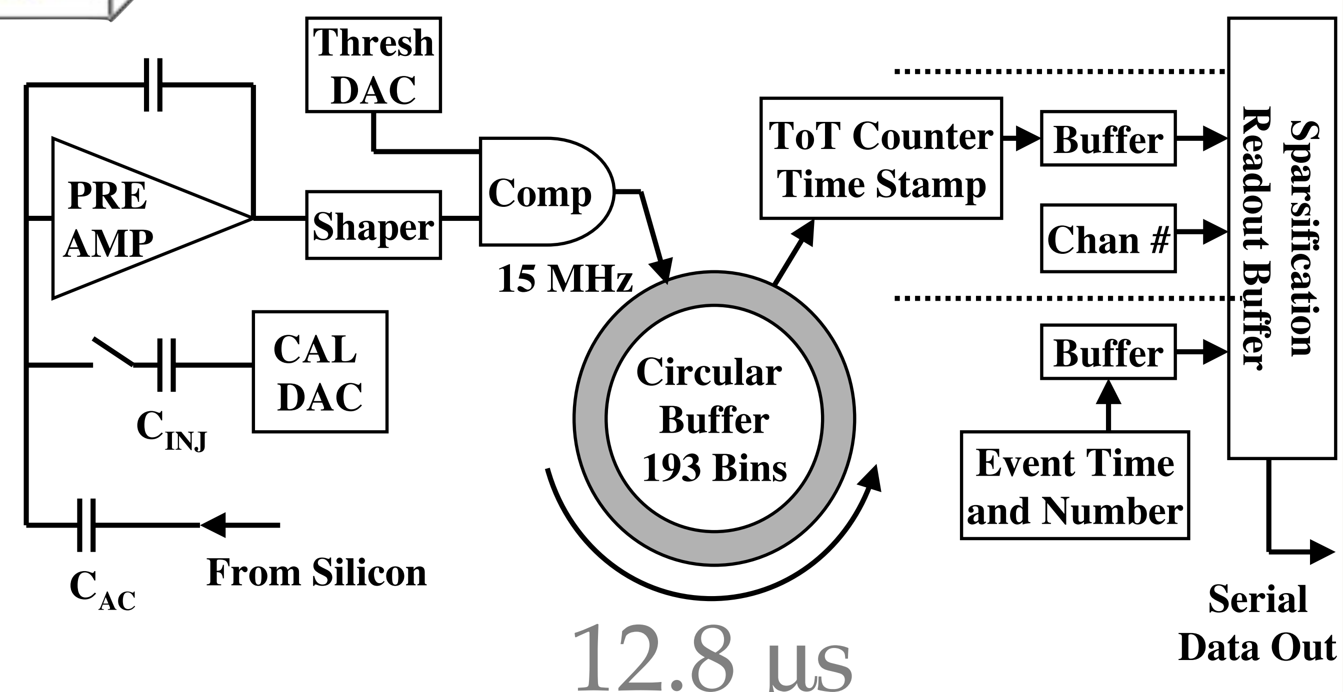

RISOLUZIONE PUNTUALE

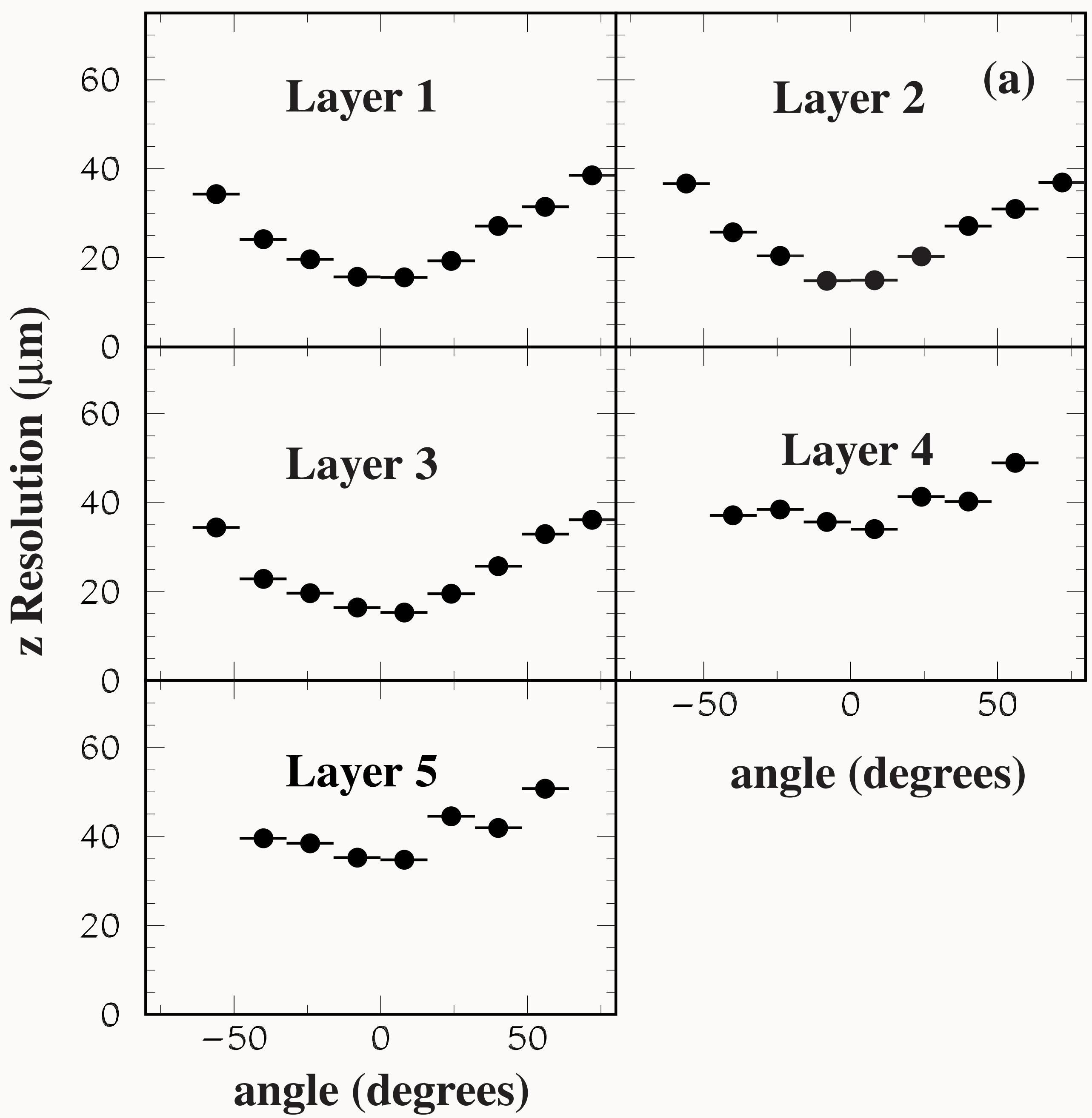

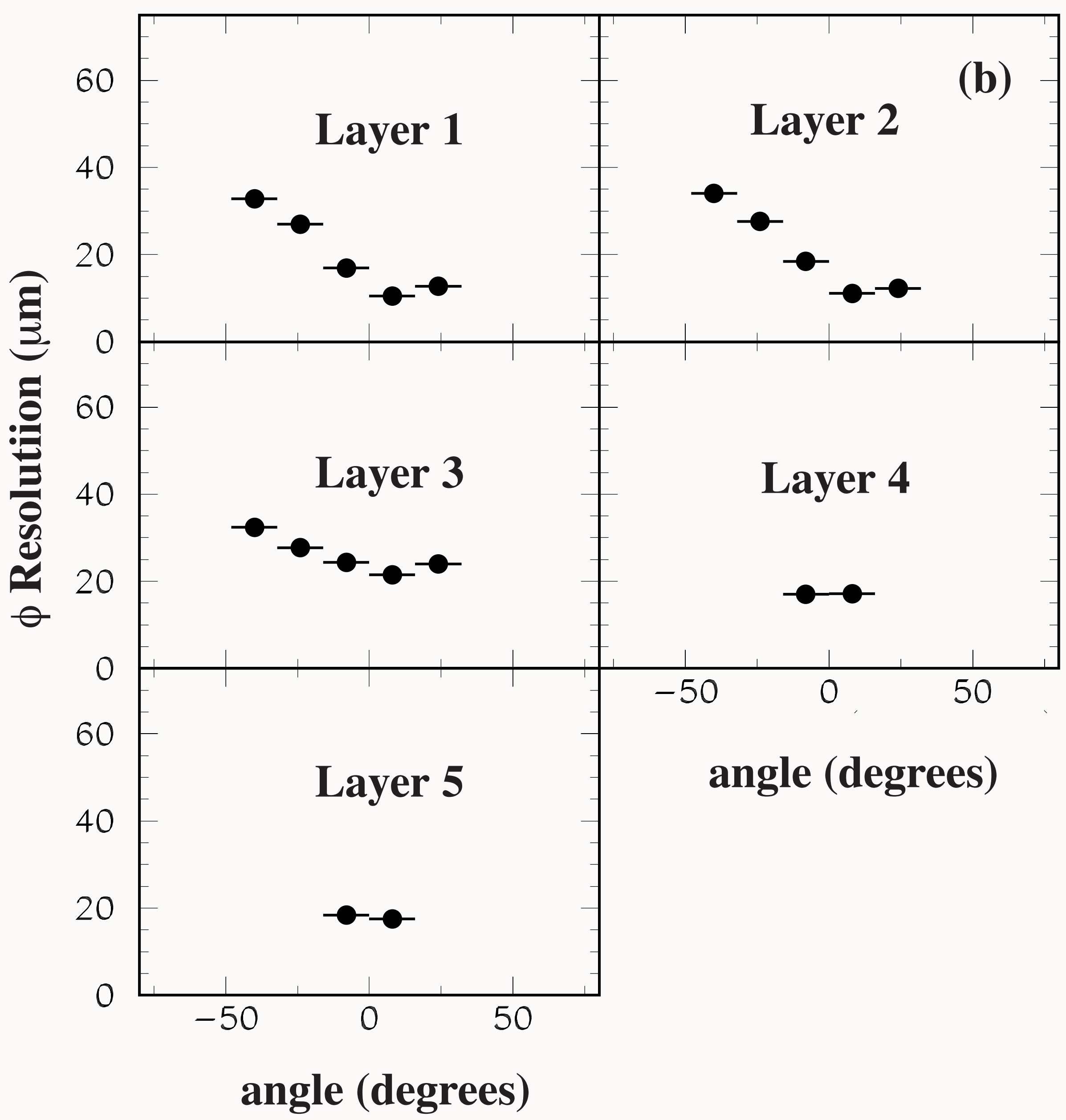

Tutto Si Muove

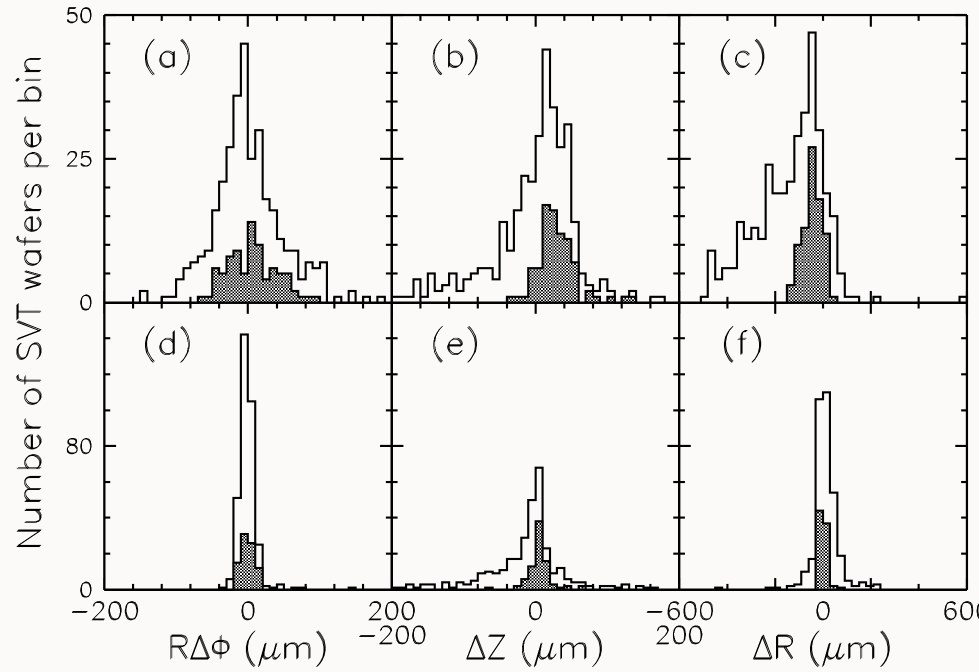

Figure 24. Comparison of a local alignment of all the sensors in the SVT using data from January 2000 with the optical survey of the SVT made during assembly in February 1999 in the (a) $r\Delta\phi$, (b) Δz and (c) Δr coordinates. Plots (d), (e), and (f) show the difference between two local alignments using data from January 15-19 and March 6-7, 2000 for the $r\Delta\phi$, Δz, and Δr coordinates, respectively. In all the plots, the shaded regions correspond to the sensors in the first three layers. In comparing the different alignments and optical survey, a six parameter fit (three global translations and three global rotations) has been applied between the data sets.

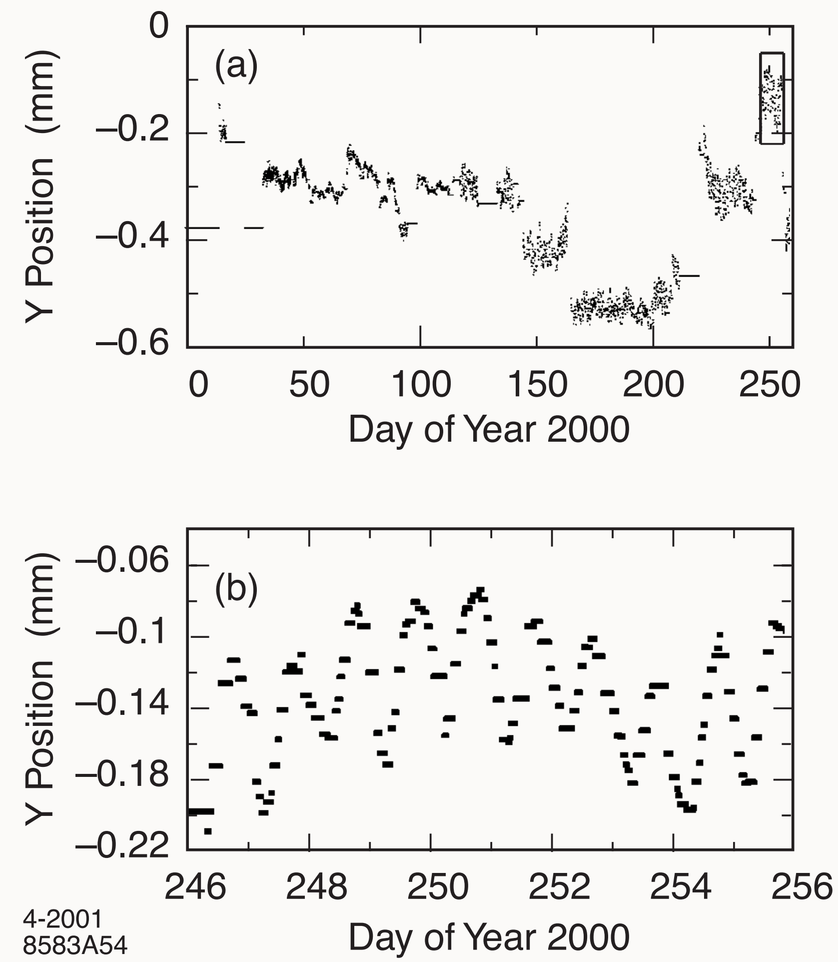

Figure 25. Global alignment of the SVT relative to the DCH based on e^+e^- and $\mu^+\mu^-$ events: changes in the relative vertical placement measured a) over the entire ten-month run in the year 2000, and b) a ten-day period, illustrating diurnal variations.

tained with the SVT-only and the DCH-only fits.

Drift Chamber

Mike Kelsey Al Lavoro Sulla DCH

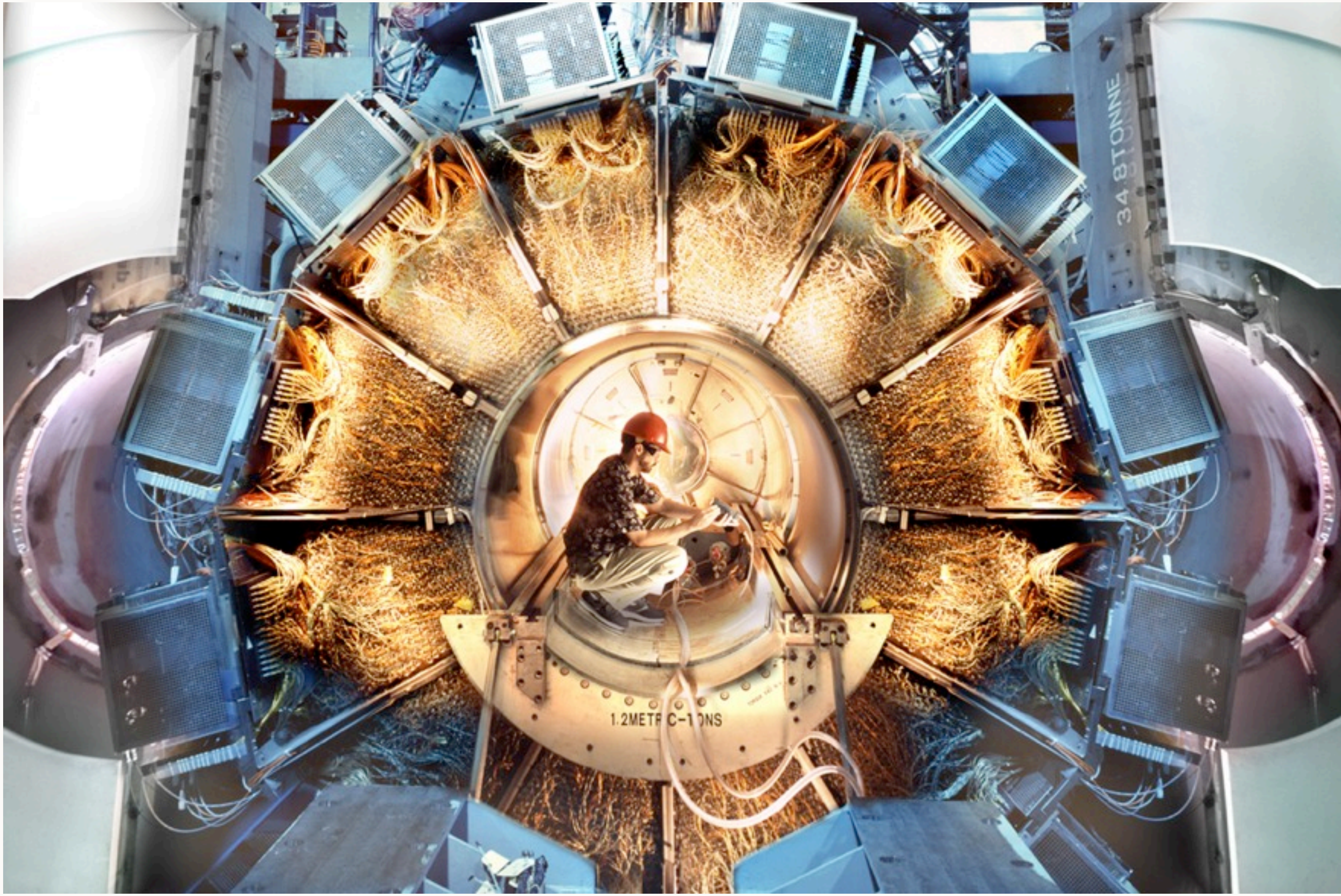

CARATTERISTICHE PRINCIPALI

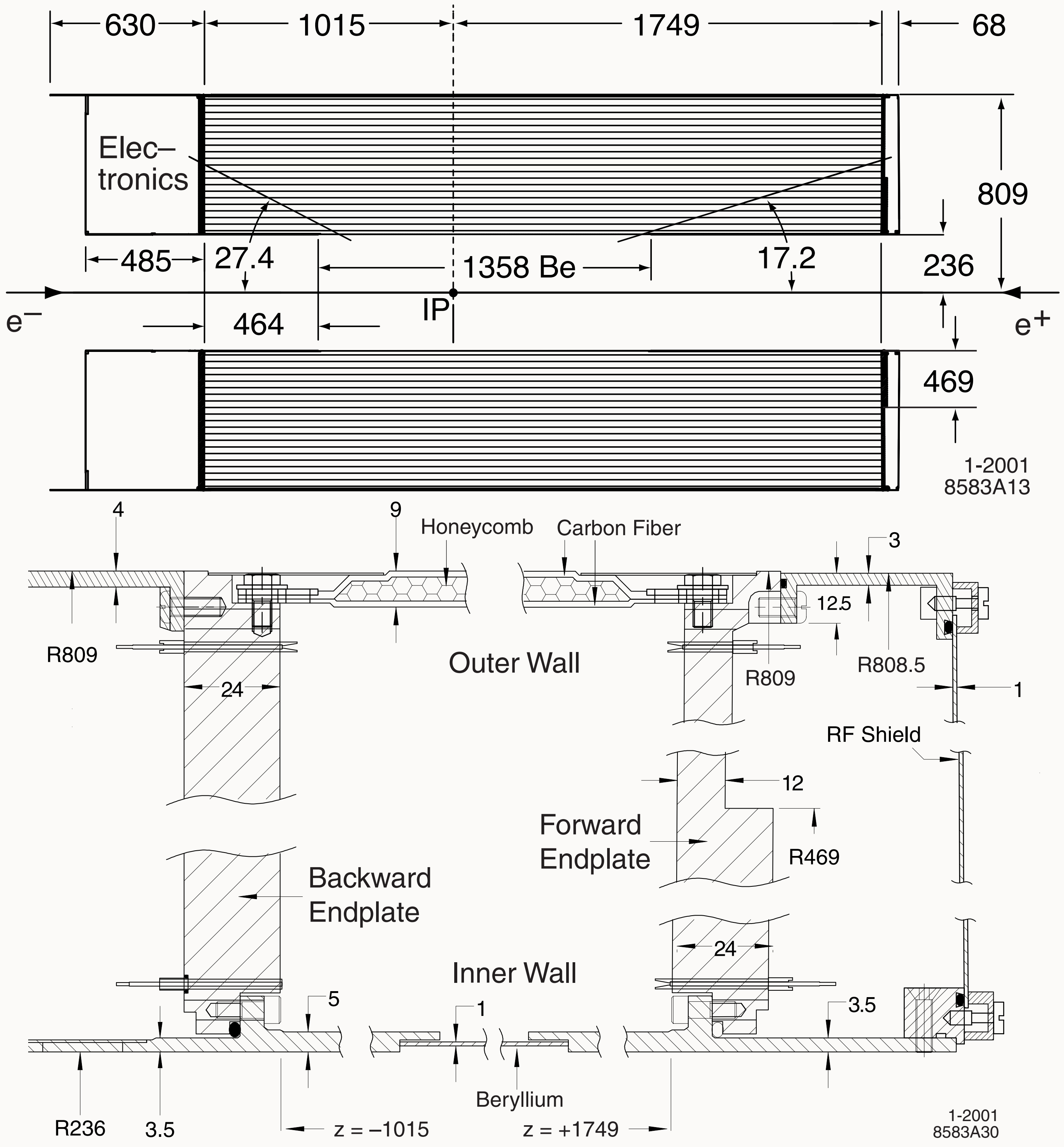

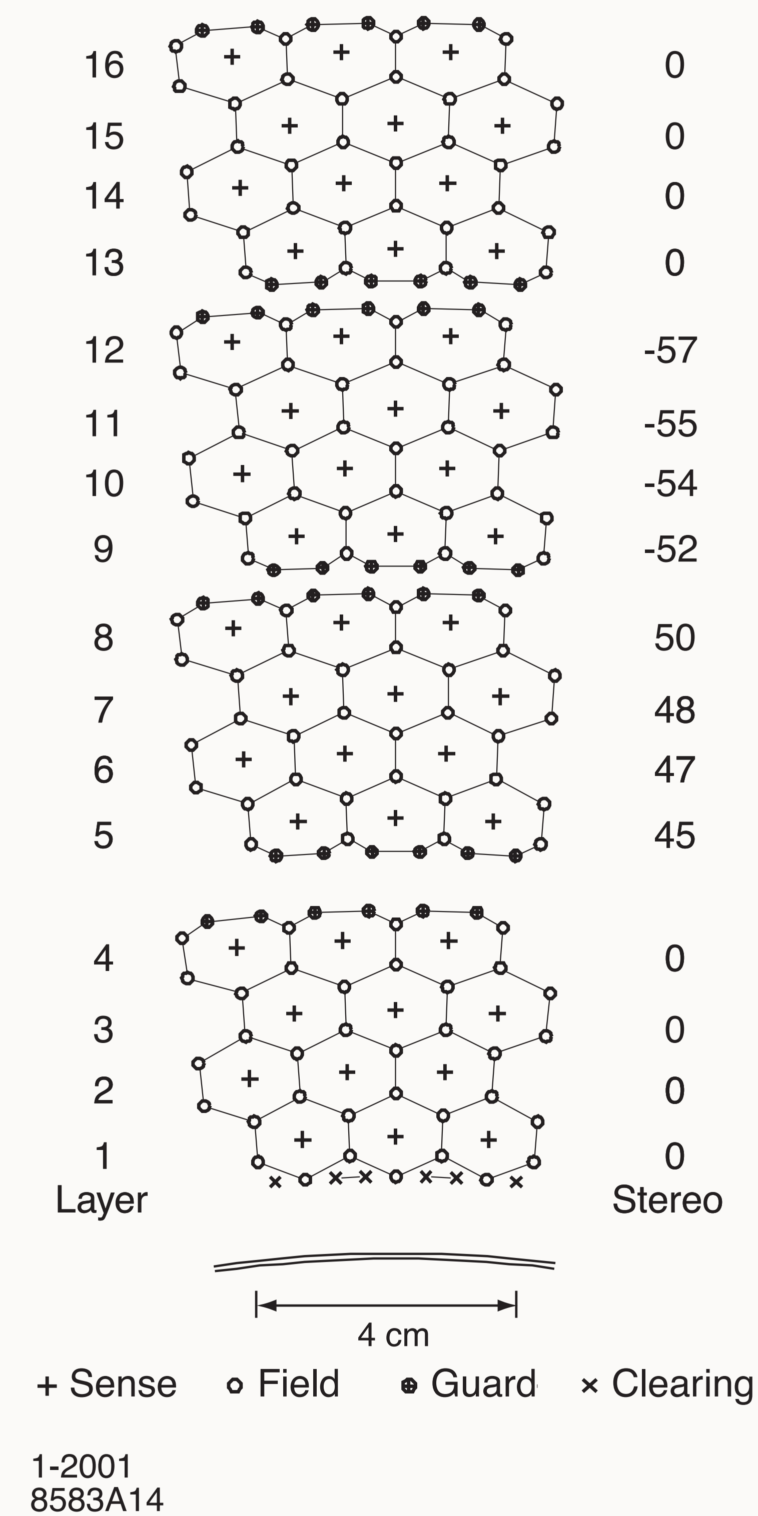

PARAMETRI

Parameter	Values
Mixture He : C_4H_{10}	80:20
Radiation Length	807 m
Primary Ions	21.2/cm
Drift Velocity	22 μm/ ns
Lorentz Angle	32°
dE/dx Resolution	6.9%

Type	Material	Diameter (μm)	Voltage (V)	Tension (g)
Sense	W-Re	20	1960	30
Field	Al	120	0	155
Guard	Al	80	340	74
Clearing	Al	120	825	155

SL	# of Cells	Radius (mm)	Width (mm)	Angle (mrad)
1	96	260.4	17.0-19.4	0
2	112	312.4	17.5-19.5	45-50
3	128	363.4	17.8-19.6	-(52-57)
4	144	422.7	18.4-20.0	0
5	176	476.6	16.9-18.2	56-60
6	192	526.1	17.2-18.3	-(63-57)
7	208	585.4	17.7-18.8	0
8	224	636.7	17.8-18.8	65-69
9	240	688.0	18.0-18.9	-(72-76)
10	256	747.2	18.3-19.2	0

Isocrone di 100 ns in 100 ns

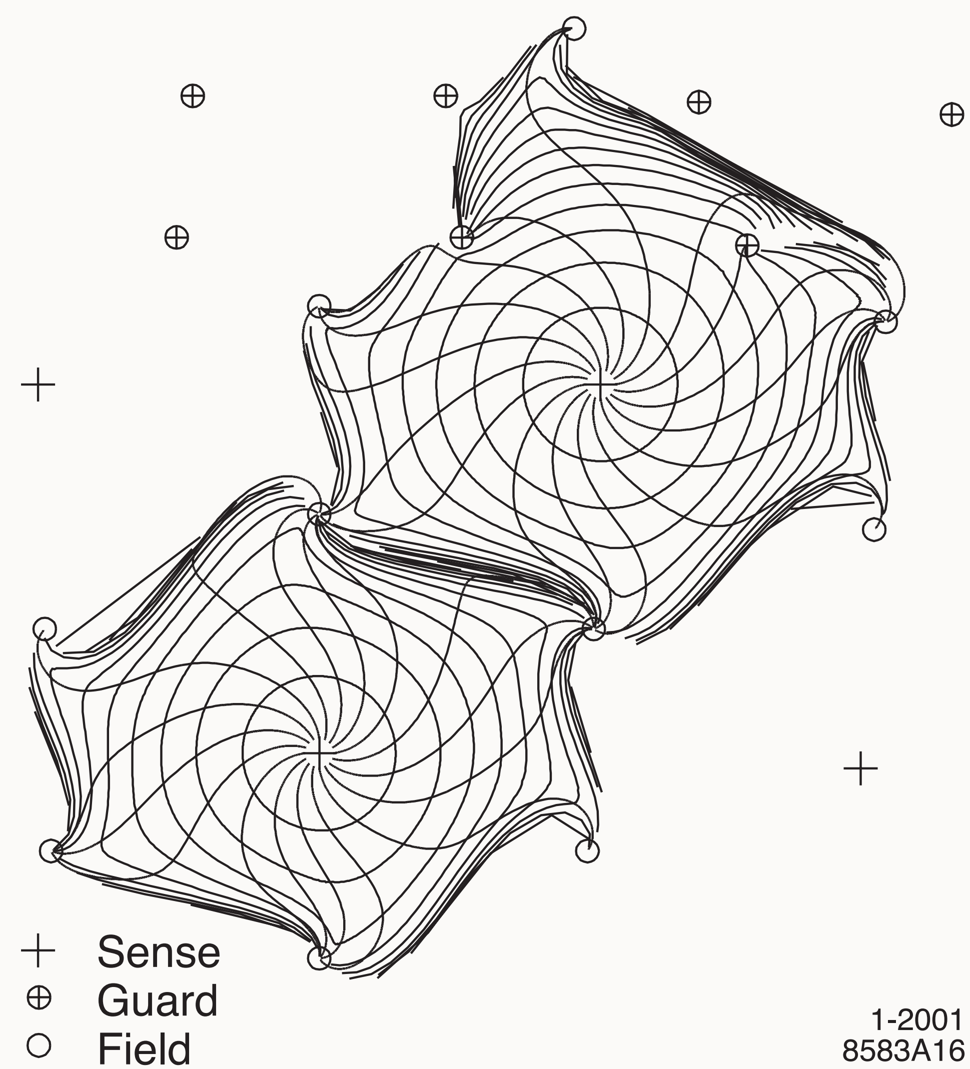

PRESTAZIONI

Risoluzione puntuale

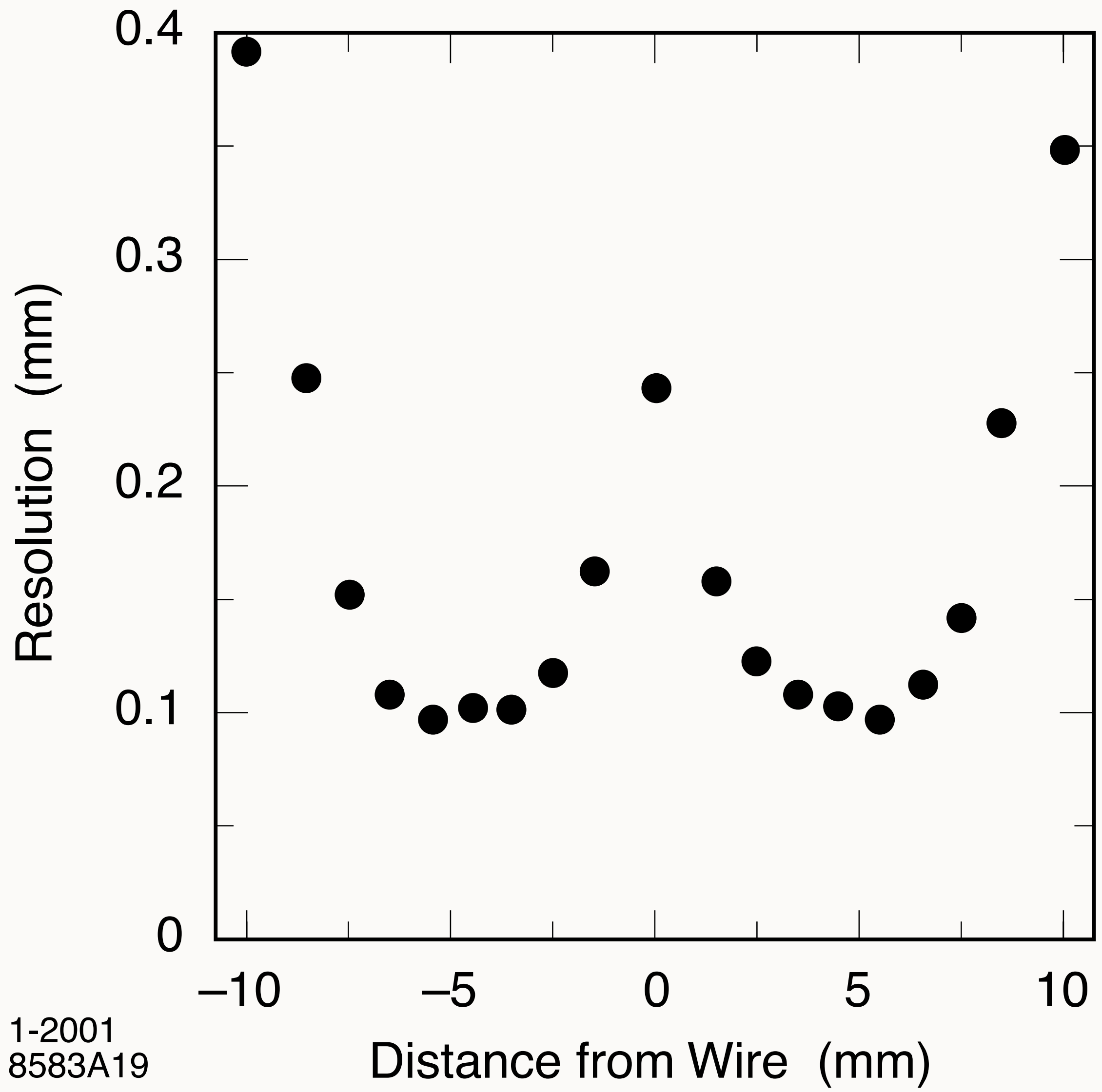

Bethe Bloch

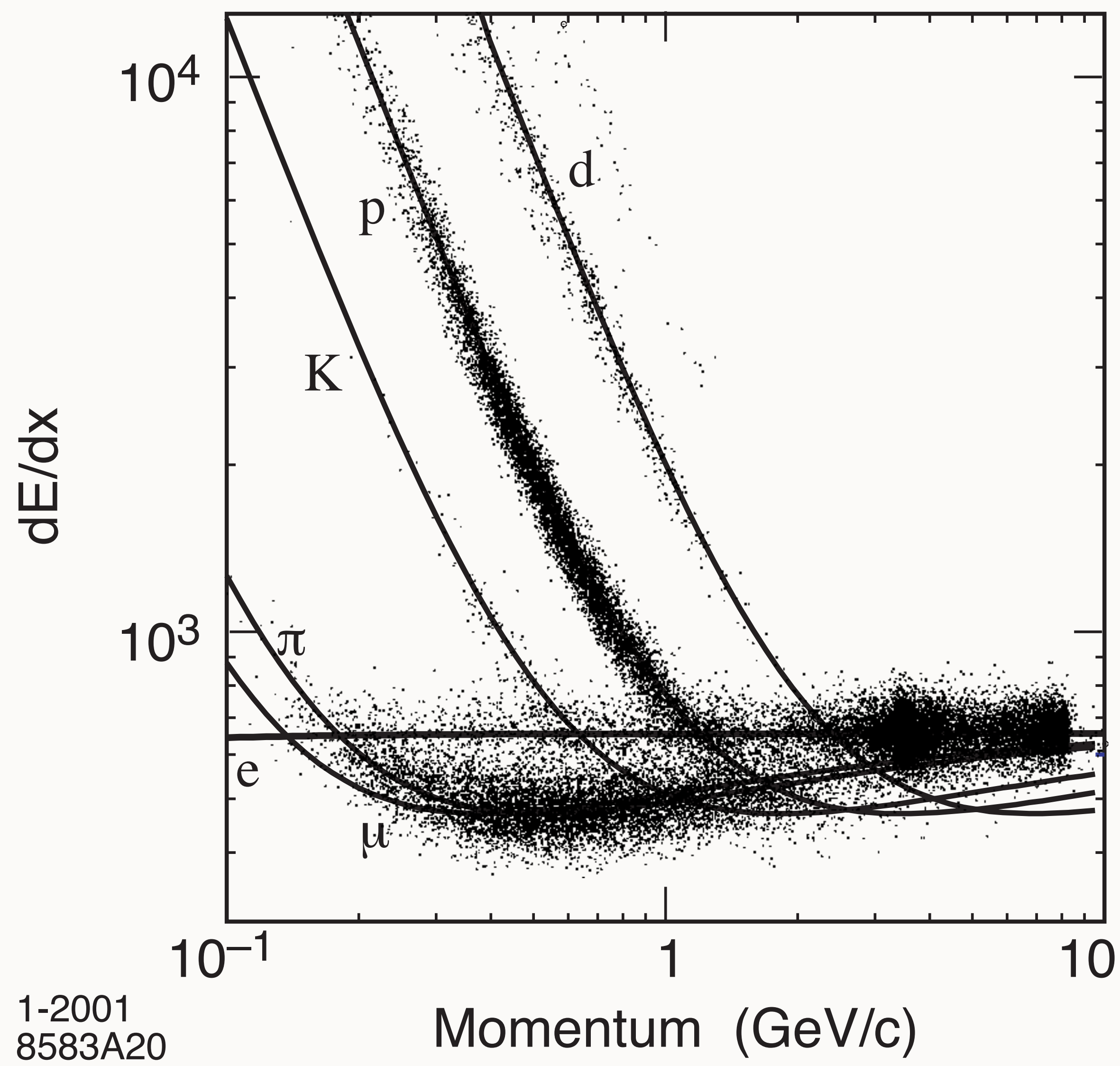

TRACKING

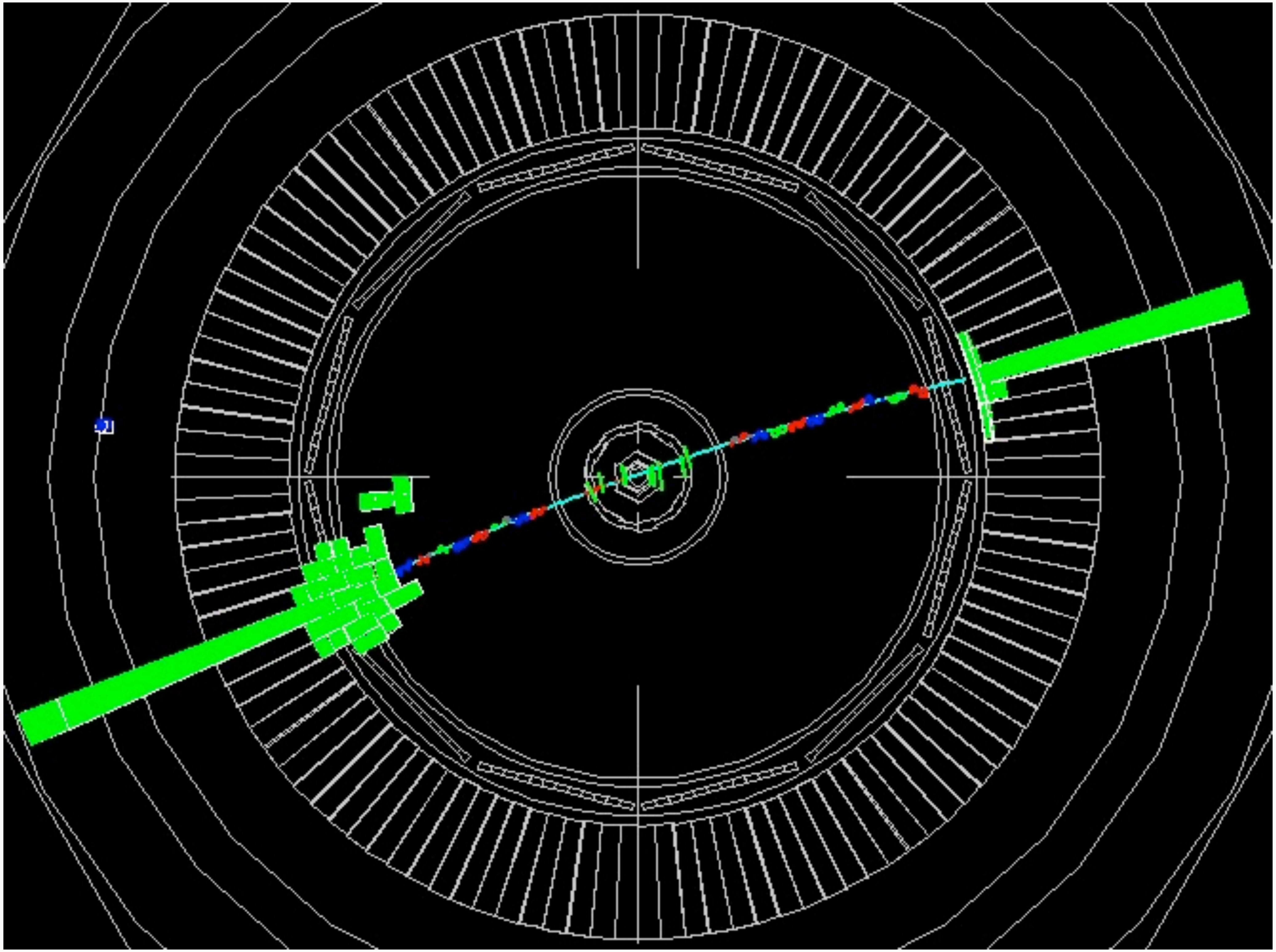

TRACKING

- Pattern Recognition
  - ....
- Kalman fit dei parametri delle tracce
  - ....

PRESTAZIONI: EFFICIENZA

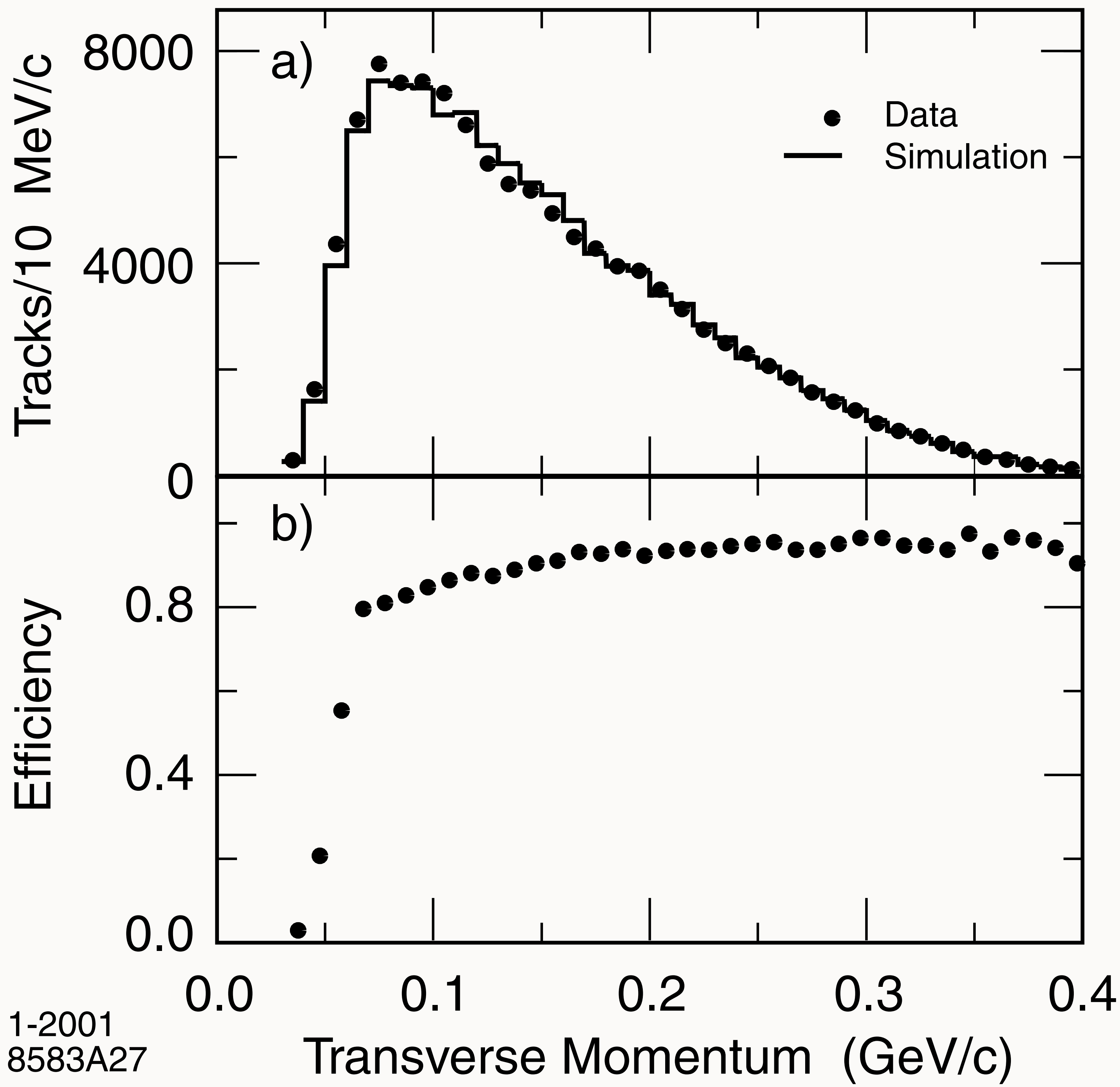

RISOLUZIONE

Da μ cosmici

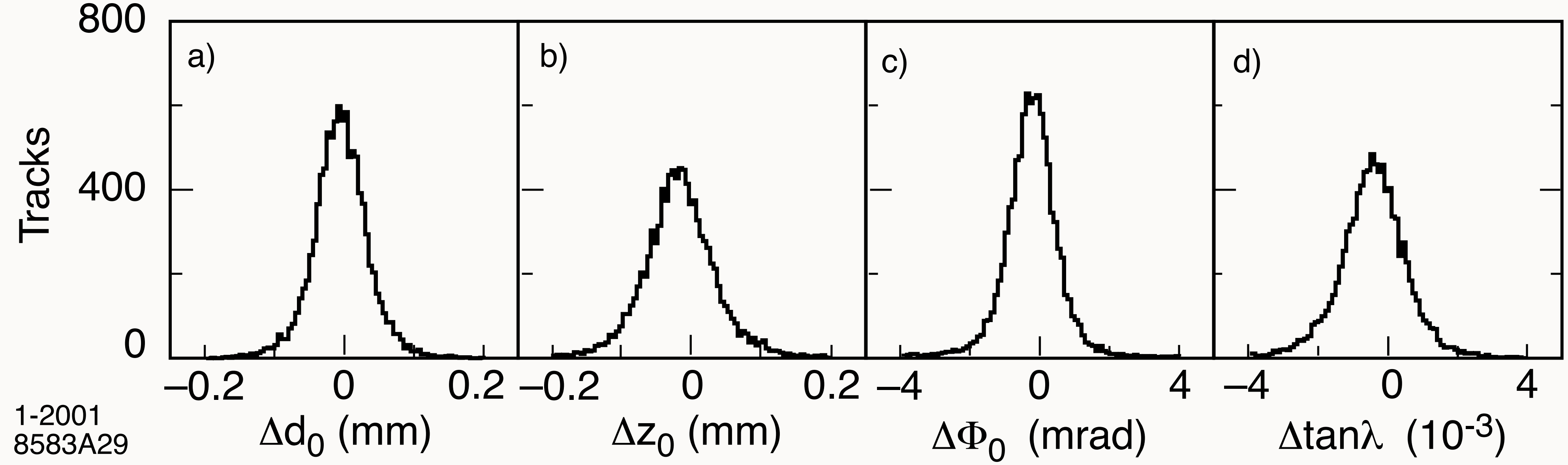

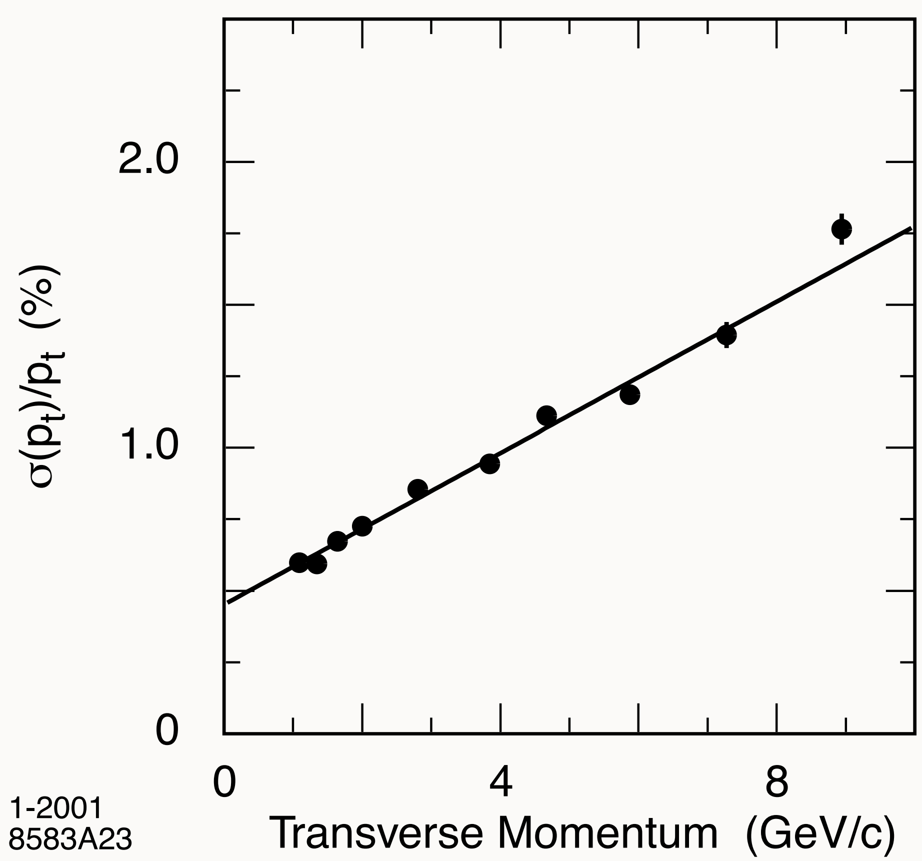

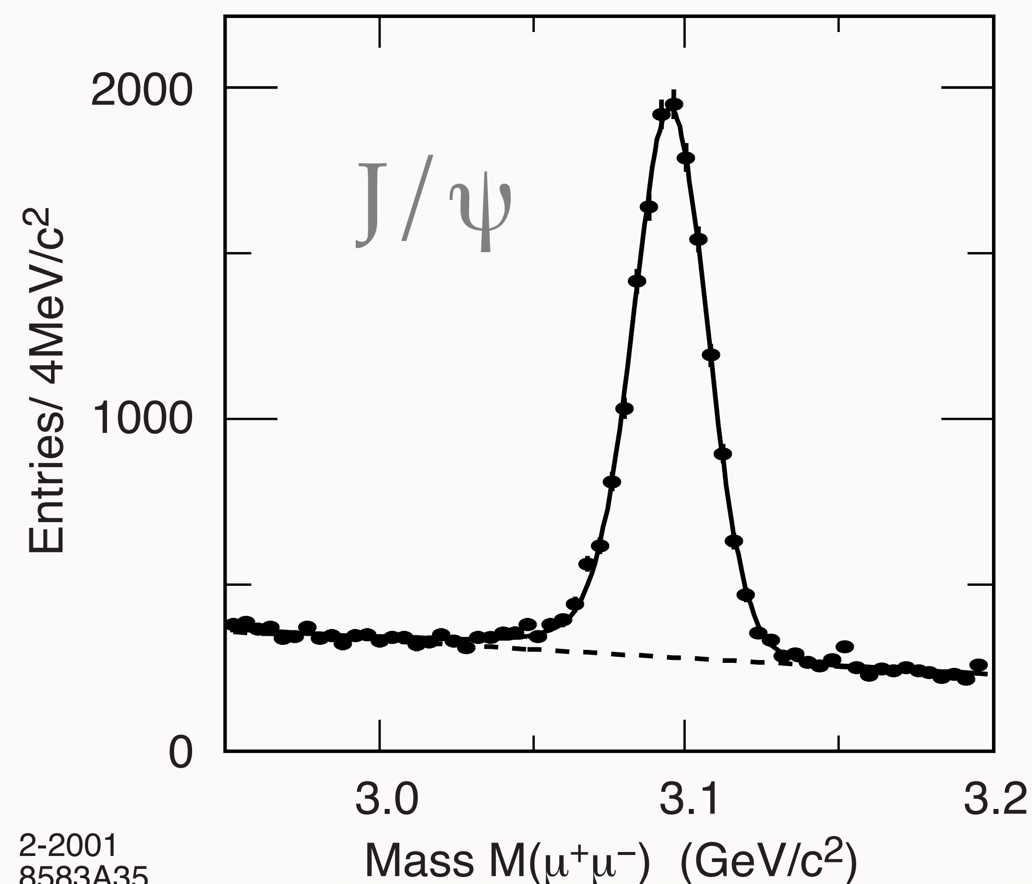

Detector of Internal Reflected Cherenkov

Jerry Va'vra e Le Sue Barre Di Quarzo

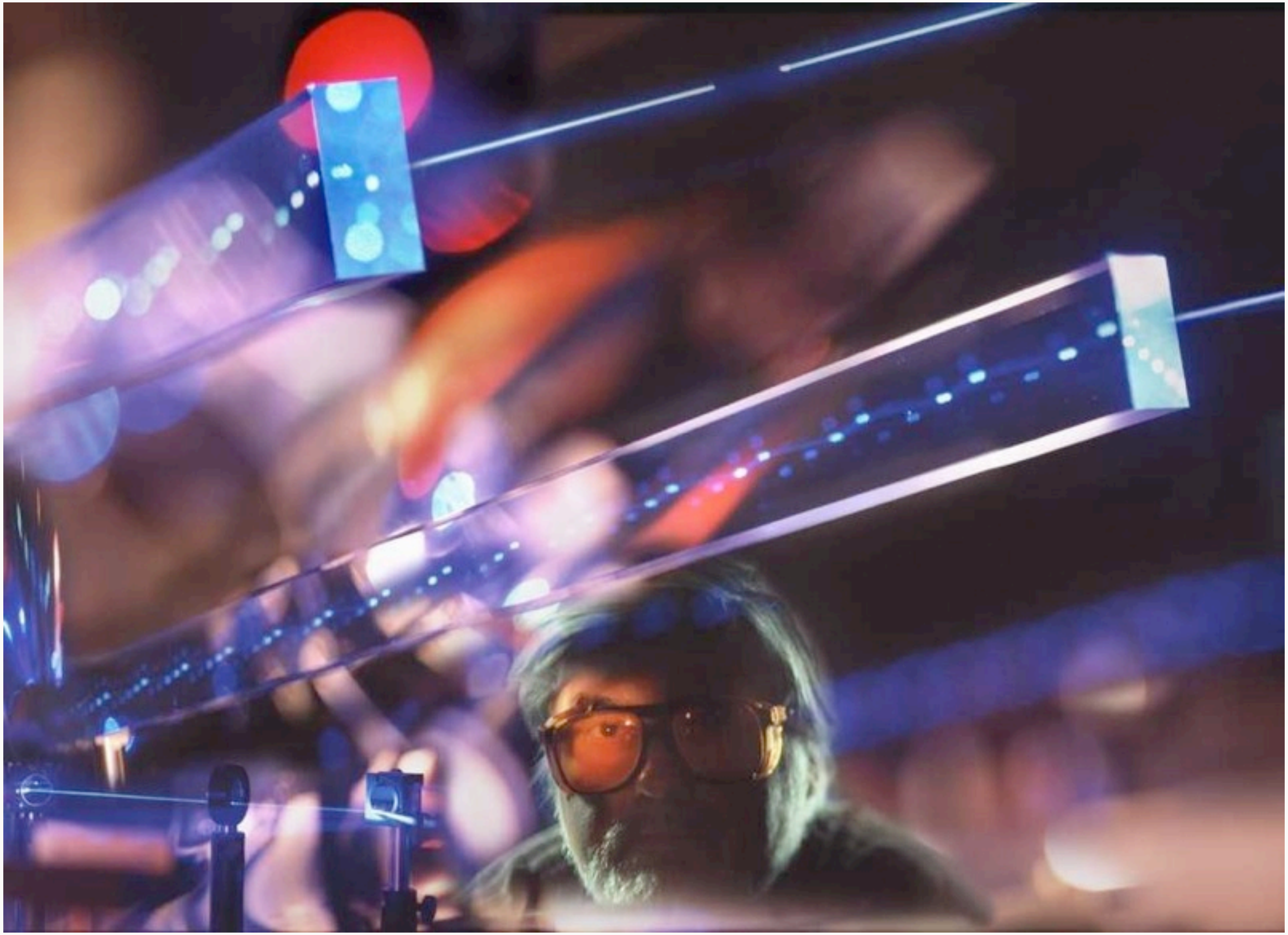

PRINCIPIO DI FUNZIONAMENTO

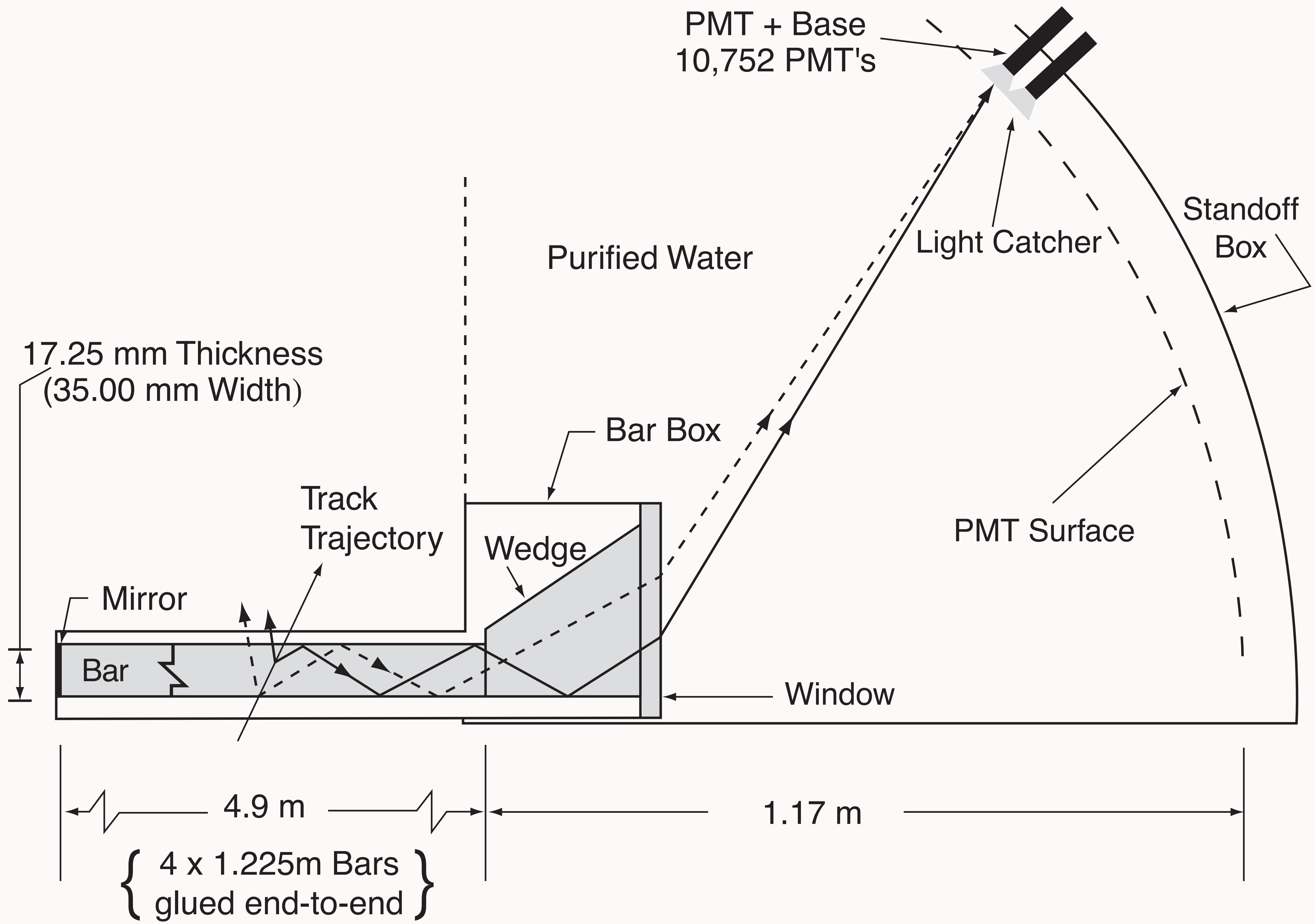

STRUTTURA MECCANICA

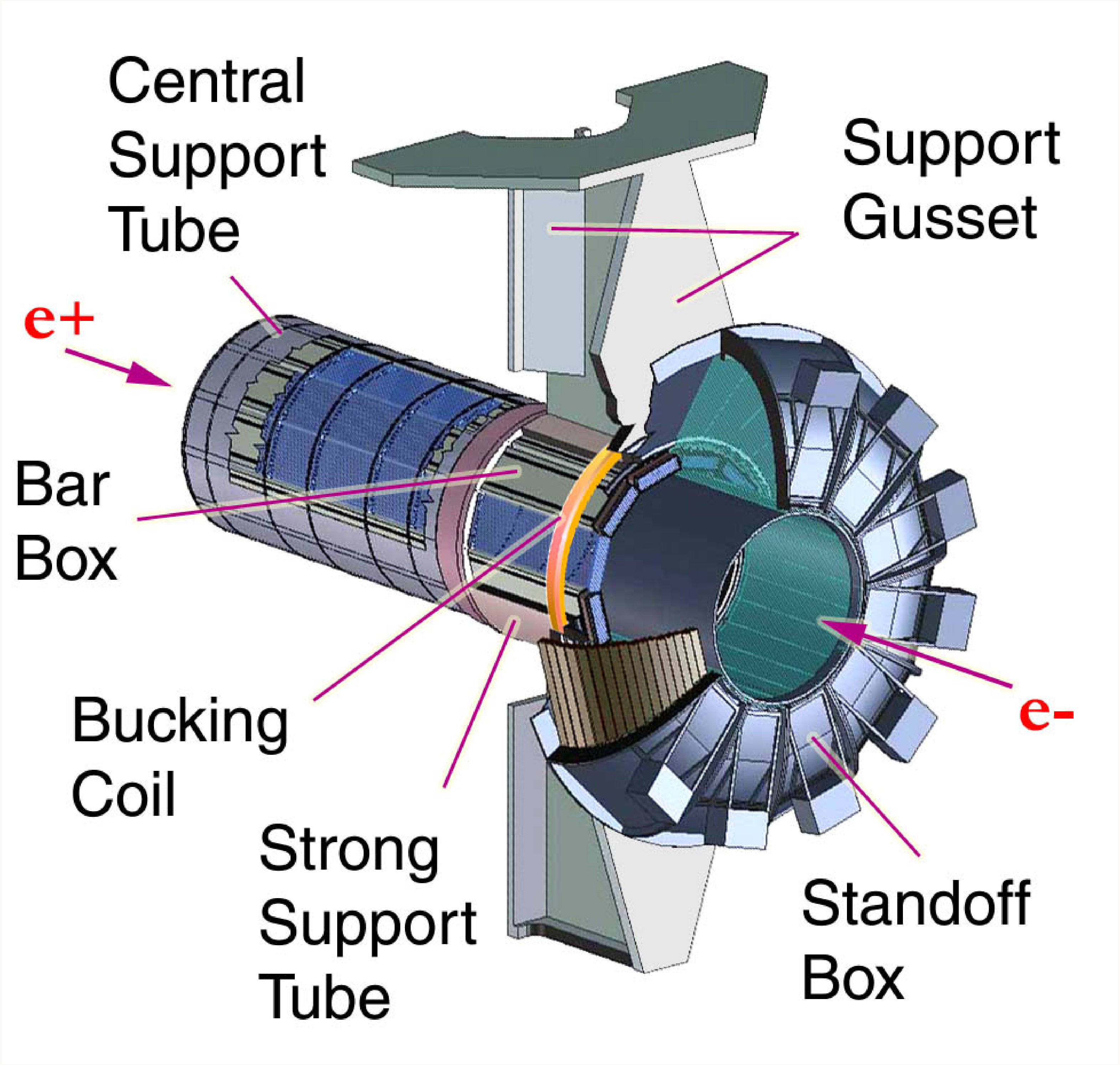

STRUTTURA MECCANICA

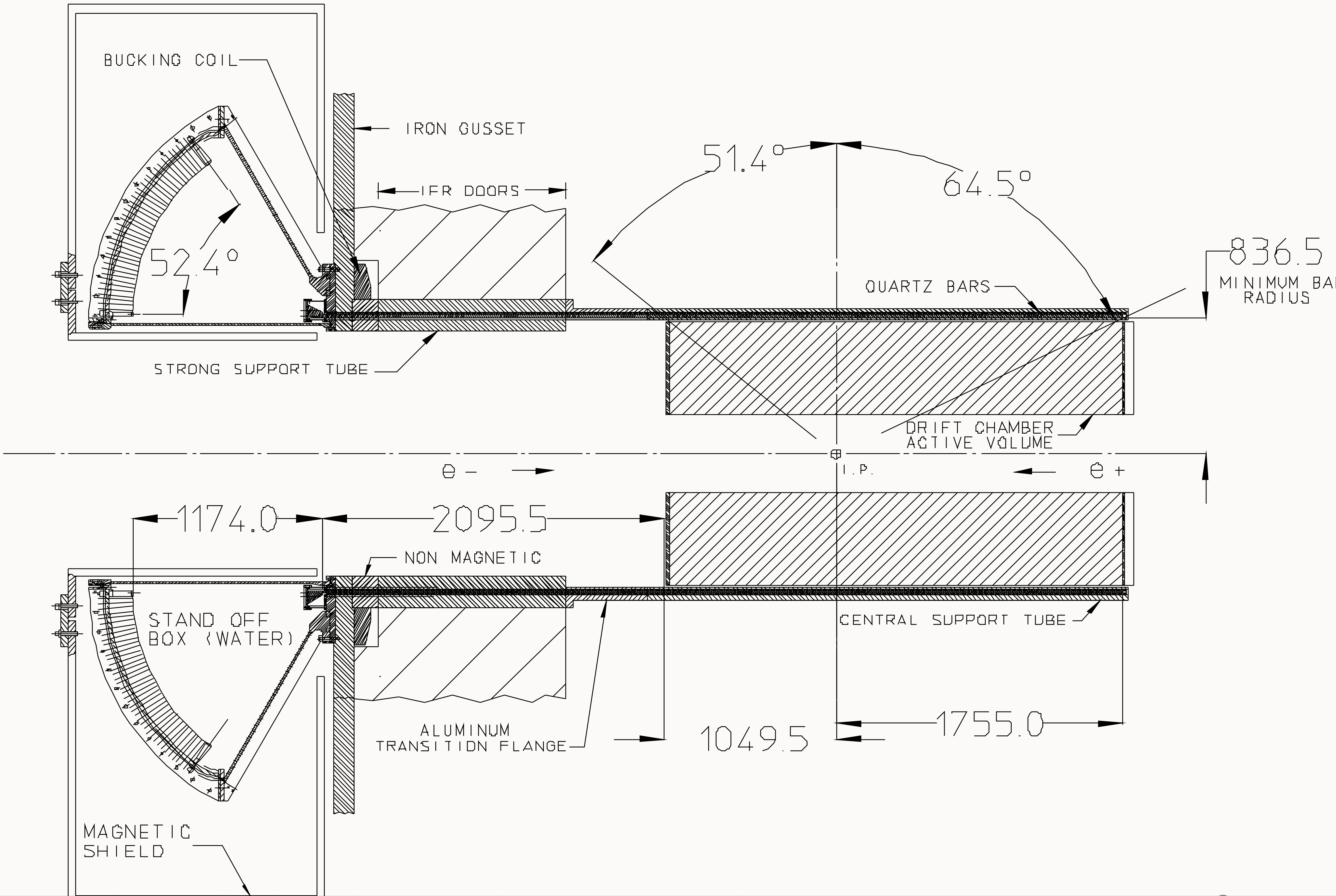

Evento e^+e^- -> Mu$^+$ Mu$^-$

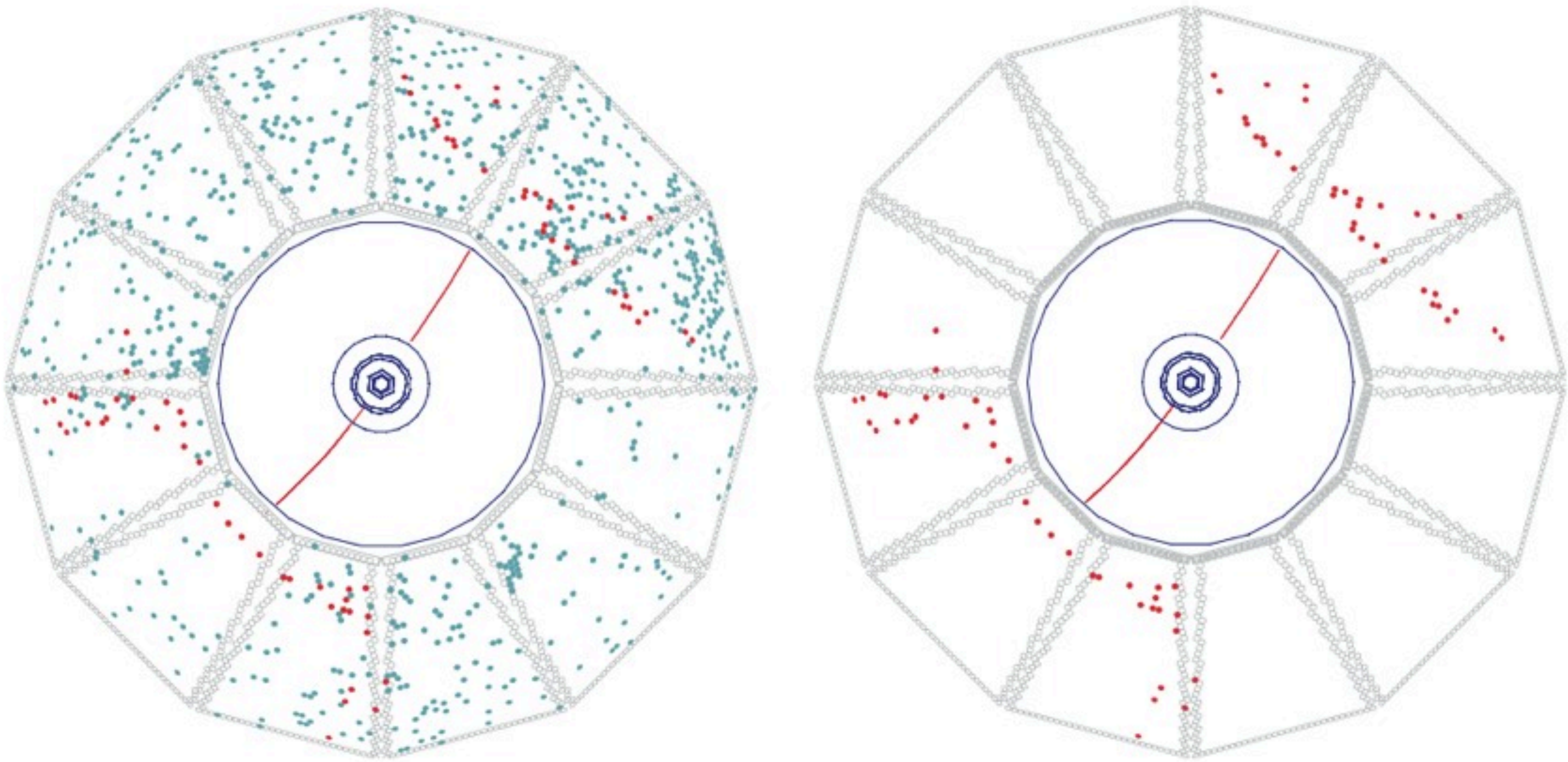

Figure 54. Display of an $e^+e^- \to \mu^+\mu^-$ event reconstructed in *BABAR* with two different time cuts. On the left, all DIRC PMTs with signals within the ± 300 ns trigger window are shown. On the right, only those PMTs with signals within 8 ns of the expected Cherenkov photon arrival time are displayed.

PRESTAZIONI

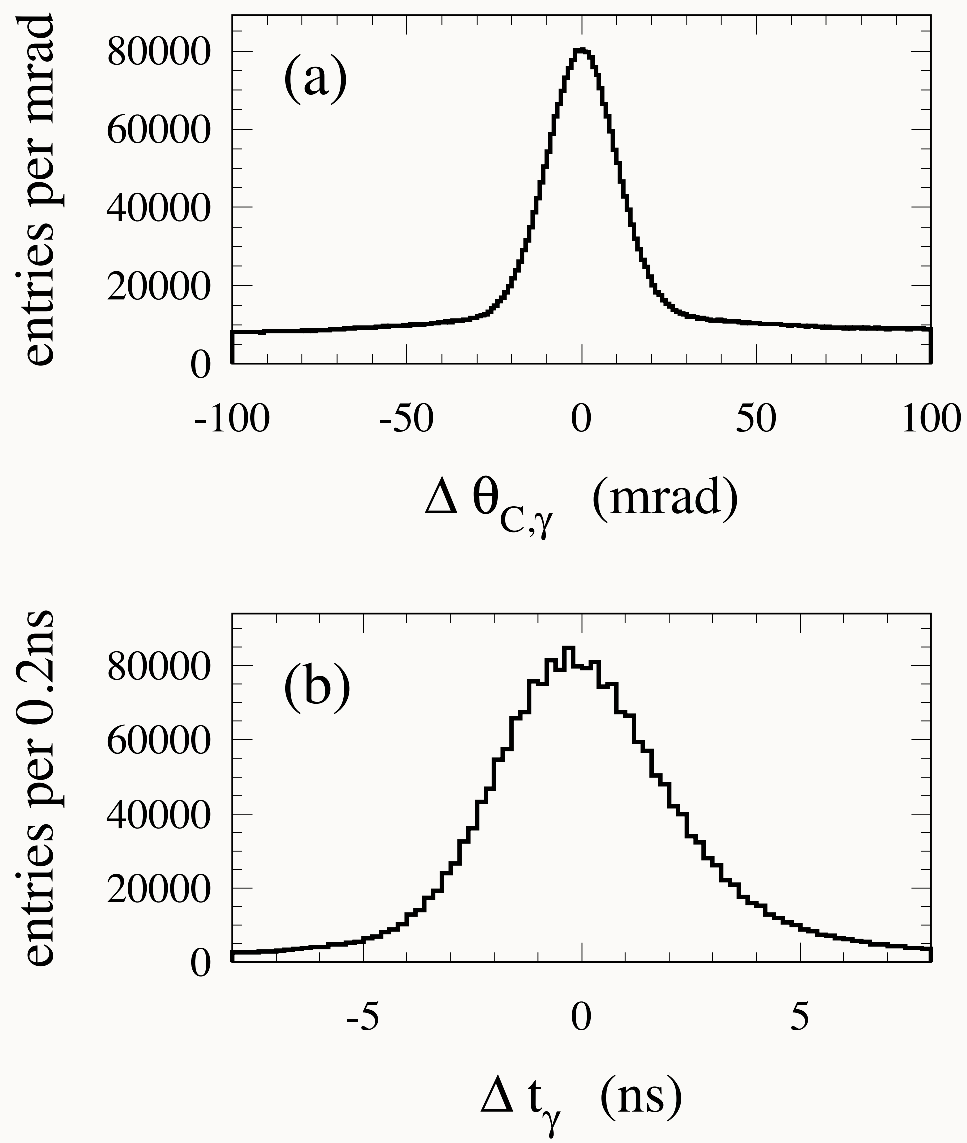

Figure 55. The difference between (a) the measured and expected Cherenkov angle for single photons, $\Delta\theta_{c,\gamma}$, and (b) the measured and expected photon arrival time, for single muons in $\mu^+\mu^-$ events.

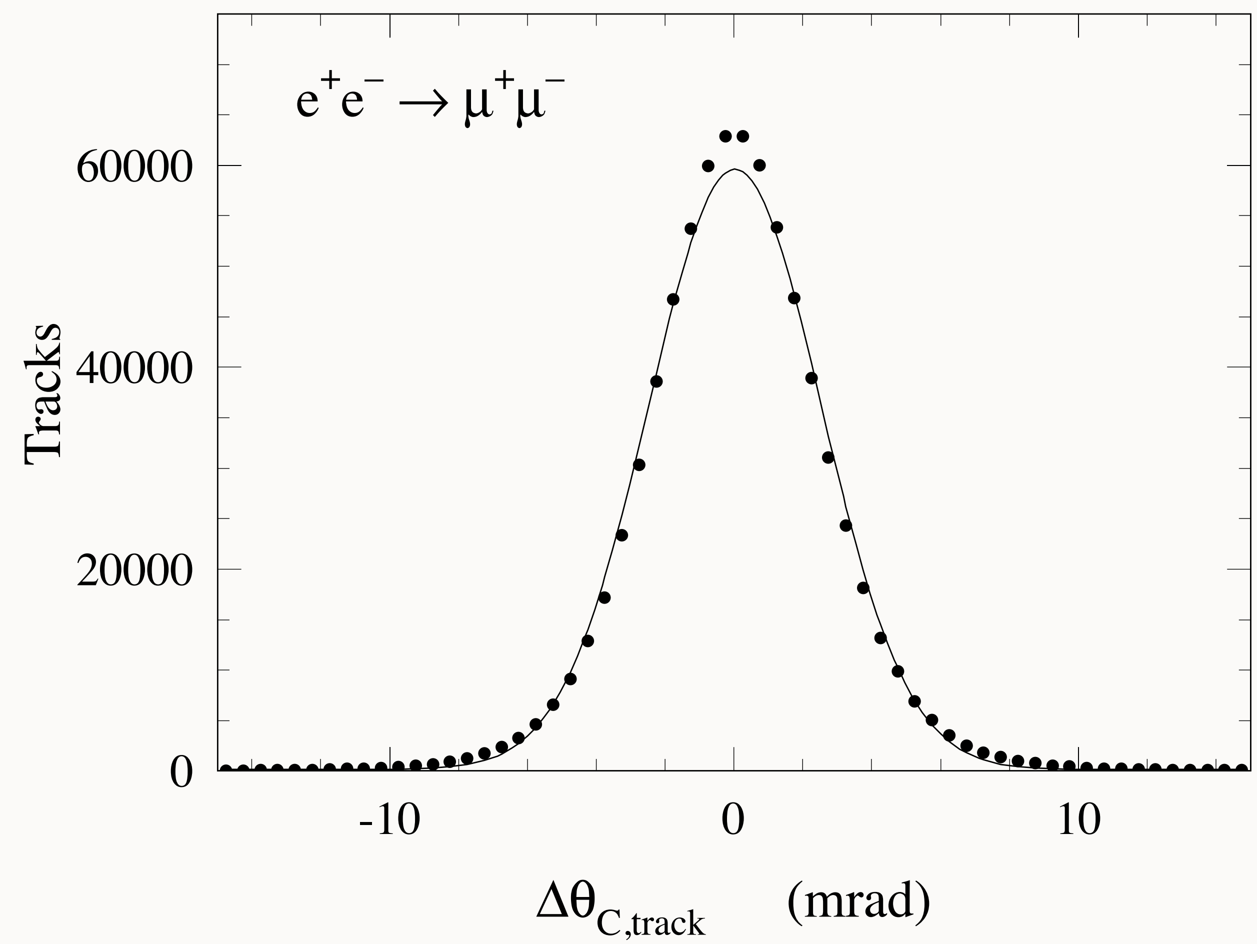

Figure 57. The difference between the measured and expected Cherenkov angle, $\Delta\theta_{c,track}$, for single muons in $\mu^+\mu^-$ events. The curve represents a Gaussian distribution fit to the data with a width of 2.5 mrad.

Ricavare: dimensione pmt e numero di fotoni rivelati

PRESTAZIONI

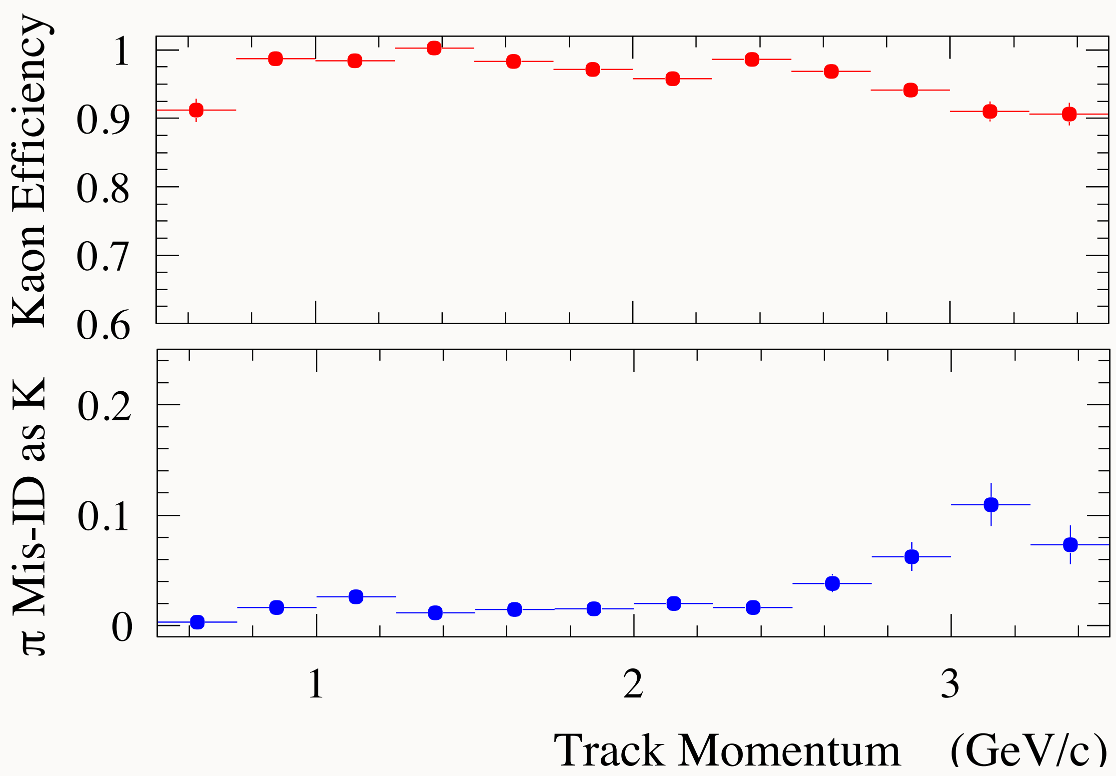

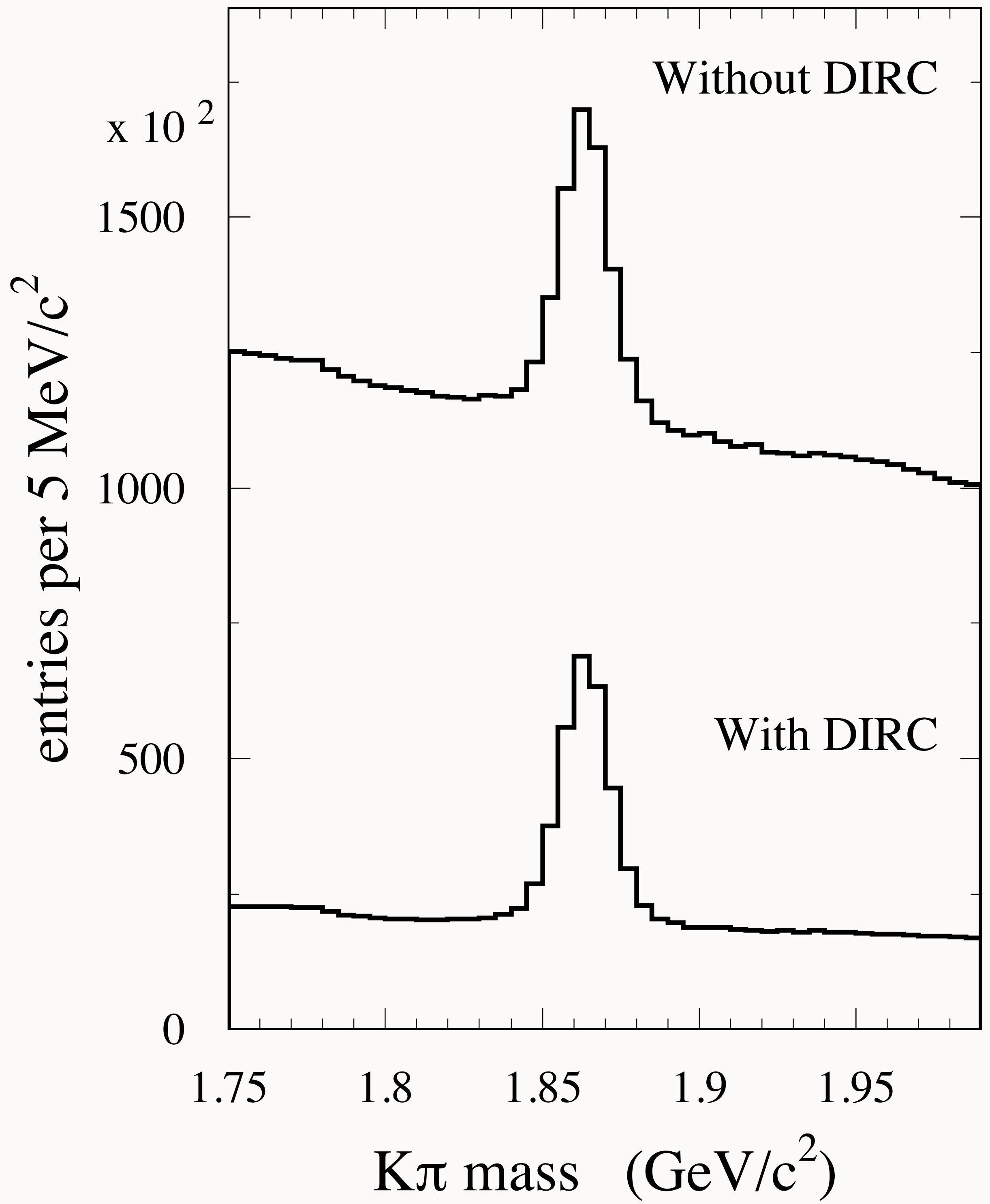

Mike Kelsey Dentro Il DIRC

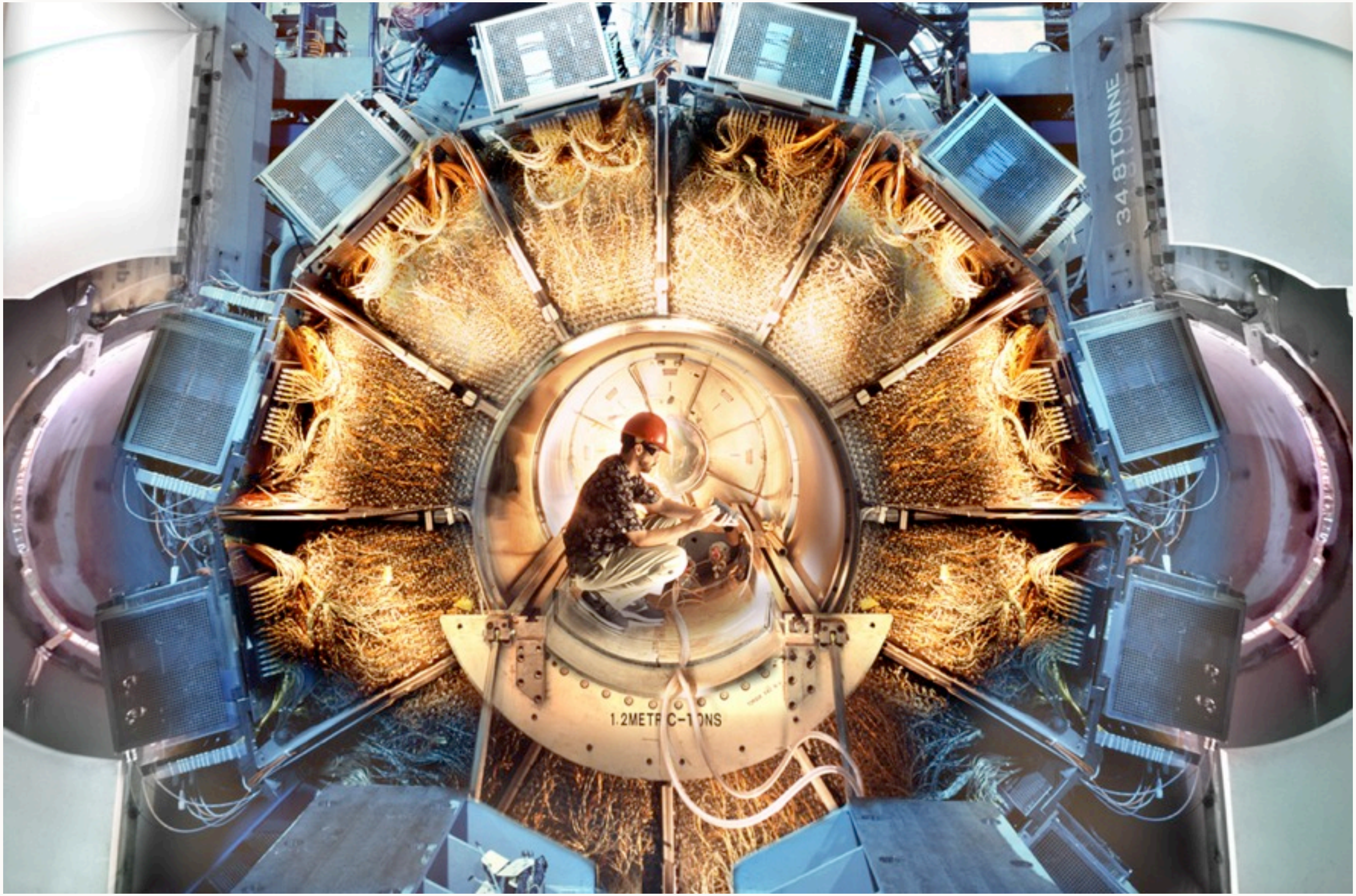

Electro Magnetic Calorimeter

CARATTERISITCHE

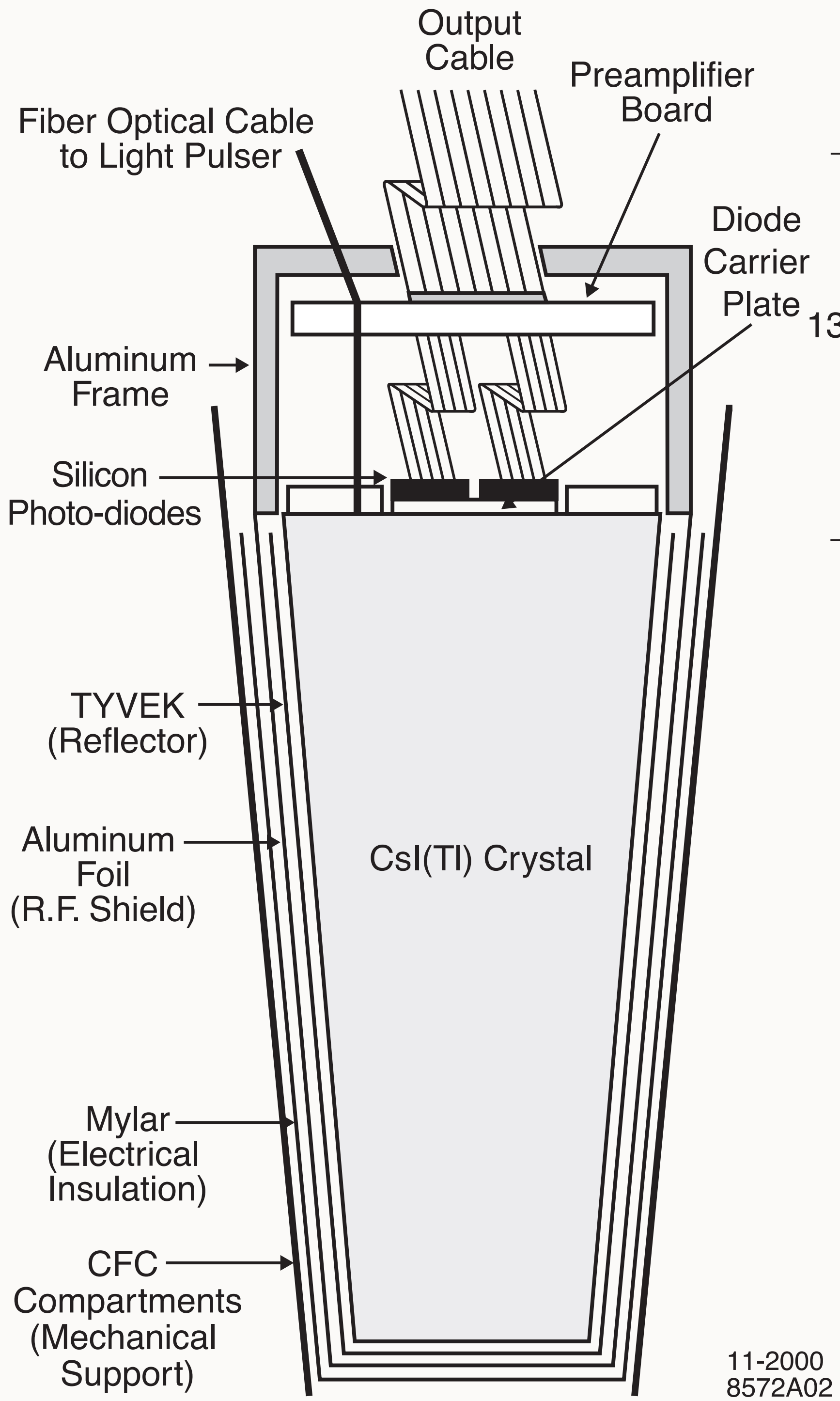

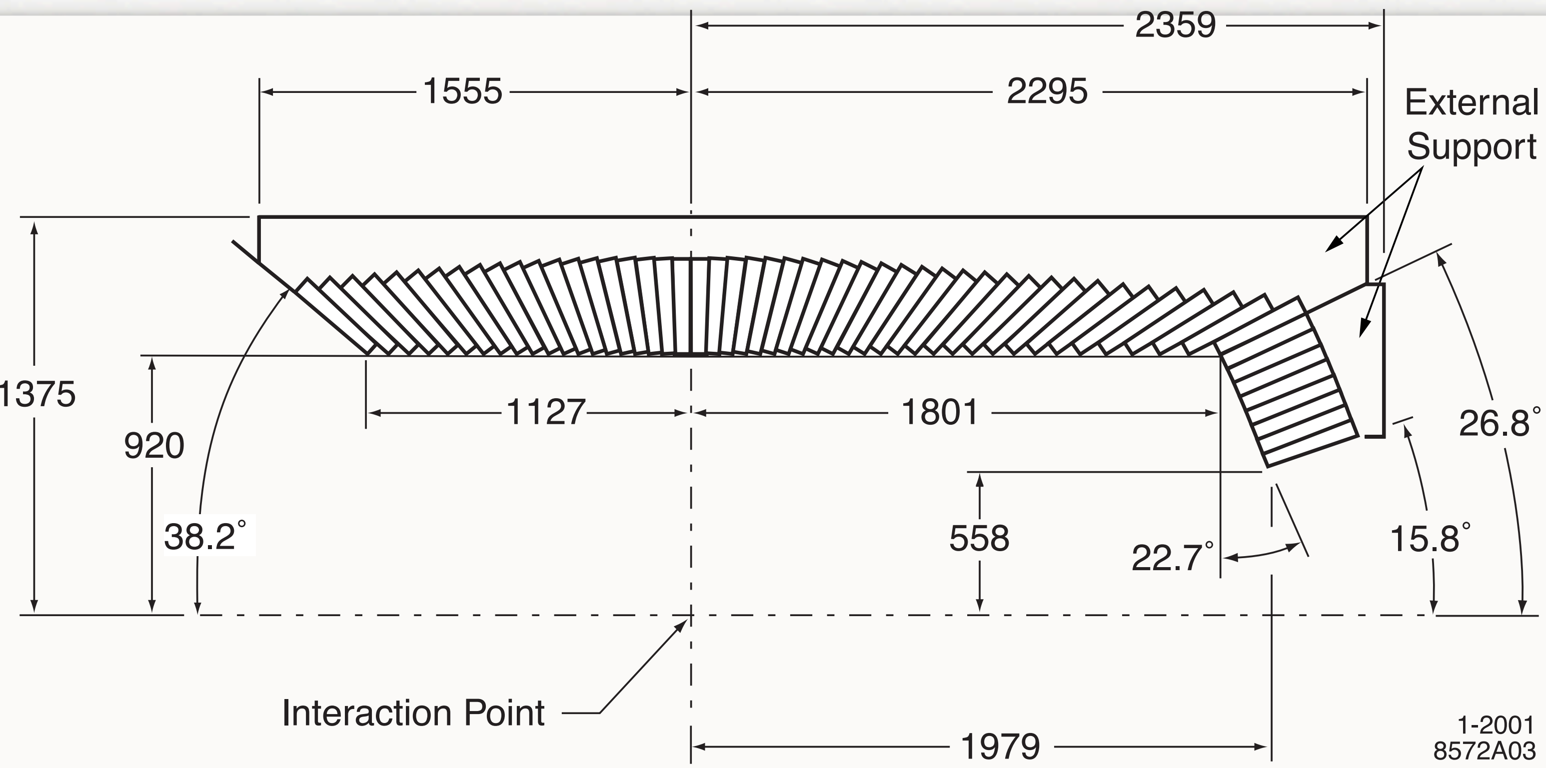

Table 11
Properties of CsI(Tl) .

Parameter	Values
Radiation Length	1.85 cm
Molière Radius	3.8 cm
Density	4.53 g/cm^3
Light Yield	50,000 γ/ MeV
Light Yield Temp. Coeff.	0.28%/°C
Peak Emission λ_{max}	565 nm
Refractive Index (λ_{max})	1.80
Signal Decay Time	680 ns (64%)
	3.34 μs (36%)

Risoluzione in Energia

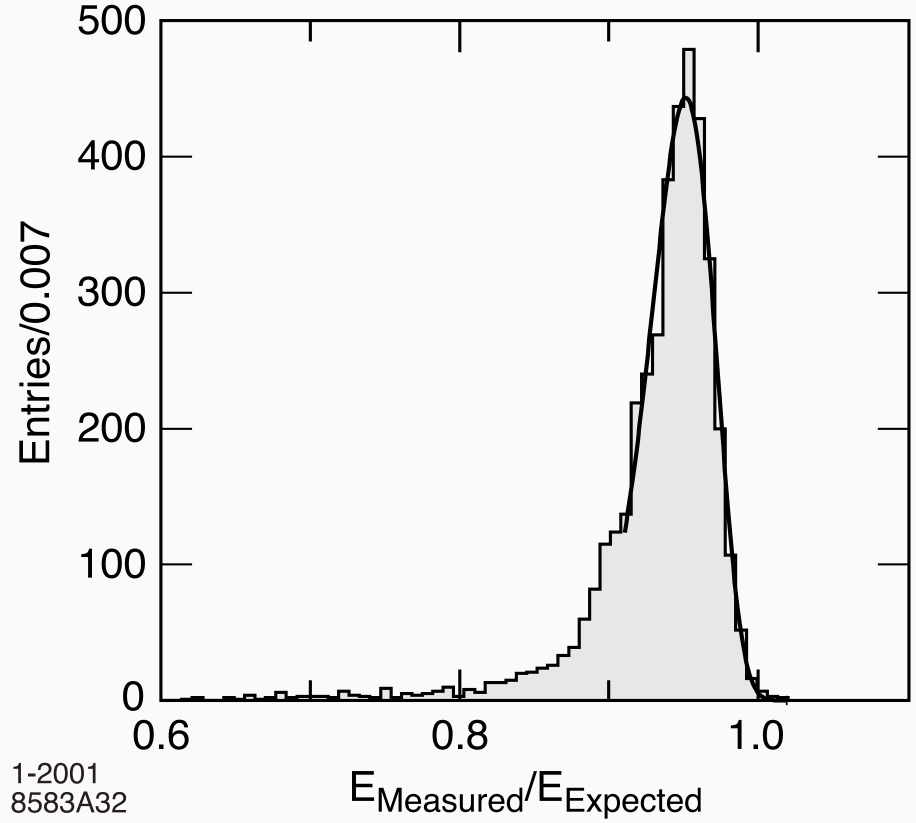

Figure 68. The ratio of the EMC measured energy to the expected energy for electrons from Bhabha scattering of 7.5 GeV/c. The solid line indicates a fit using a logarithmic function.

$$\frac{\sigma_E}{E} = \frac{(2.32 \pm 0.30)\%}{\sqrt[4]{E(\,\mathrm{GeV})}} \oplus (1.85 \pm 0.12)\%.$$

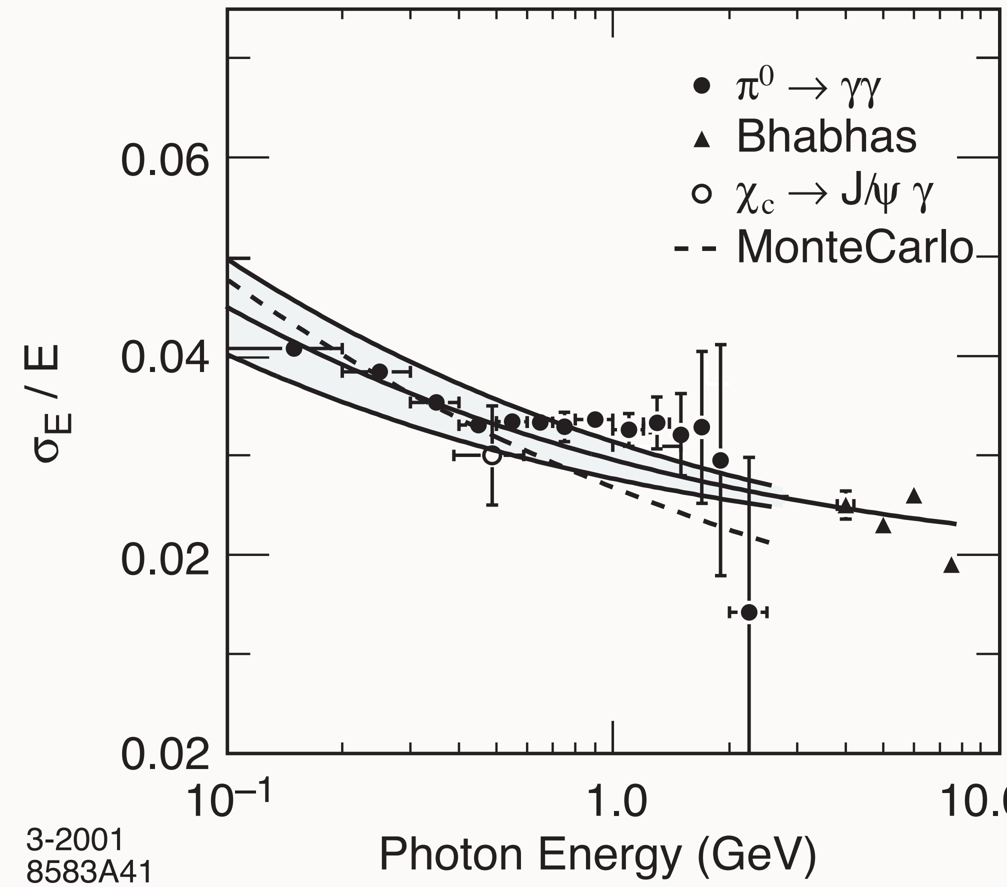

Figure 69. The energy resolution for the ECM measured for photons and electrons from various processes. The solid curve is a fit to Equation 6 and the shaded area denotes the rms error of the fit.

Risoluzione Angolare

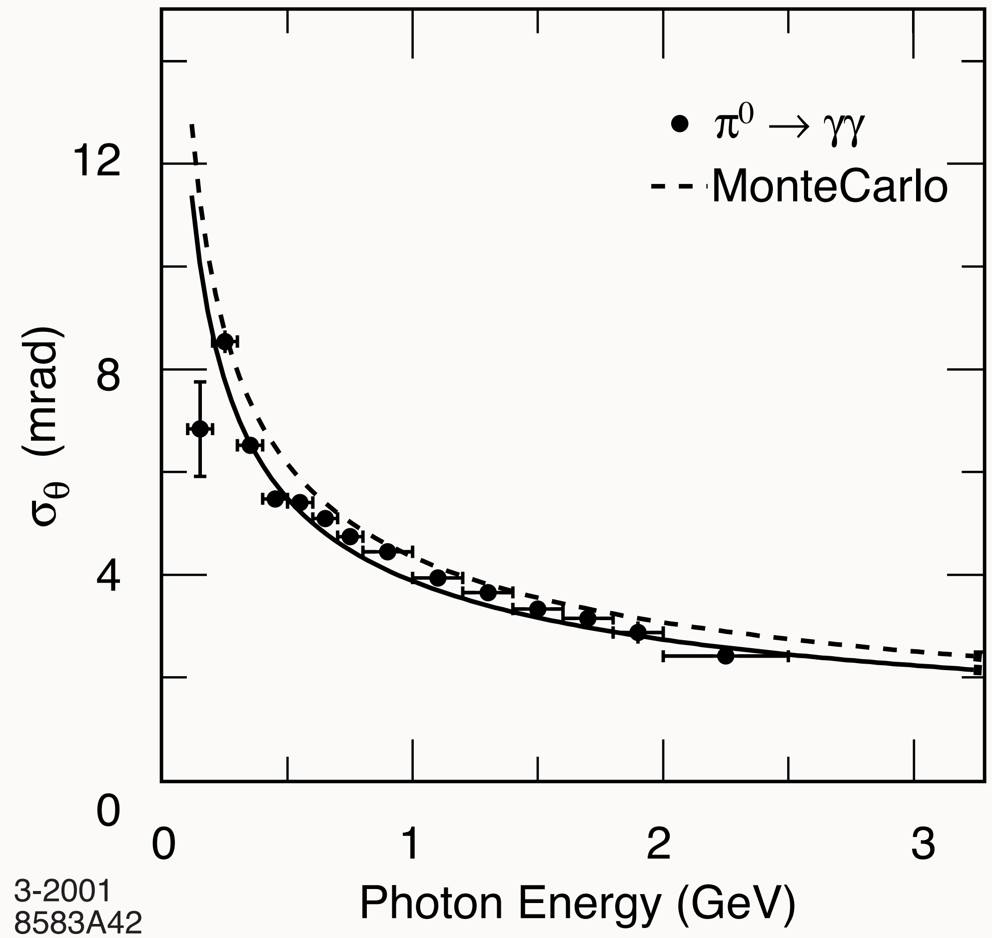

Figure 70. The angular resolution of the EMC for photons from π^0 decays. The solid curve is a fit to Equation 7.

$$\begin{aligned} \sigma_\theta &= \sigma_\phi \\ &= \left(\frac{3.87 \pm 0.07}{\sqrt{E(\,\mathrm{GeV})}} + 0.00 \pm 0.04\right) \text{ mrad.} \end{aligned} \quad (10)$$

PRESTAZIONI

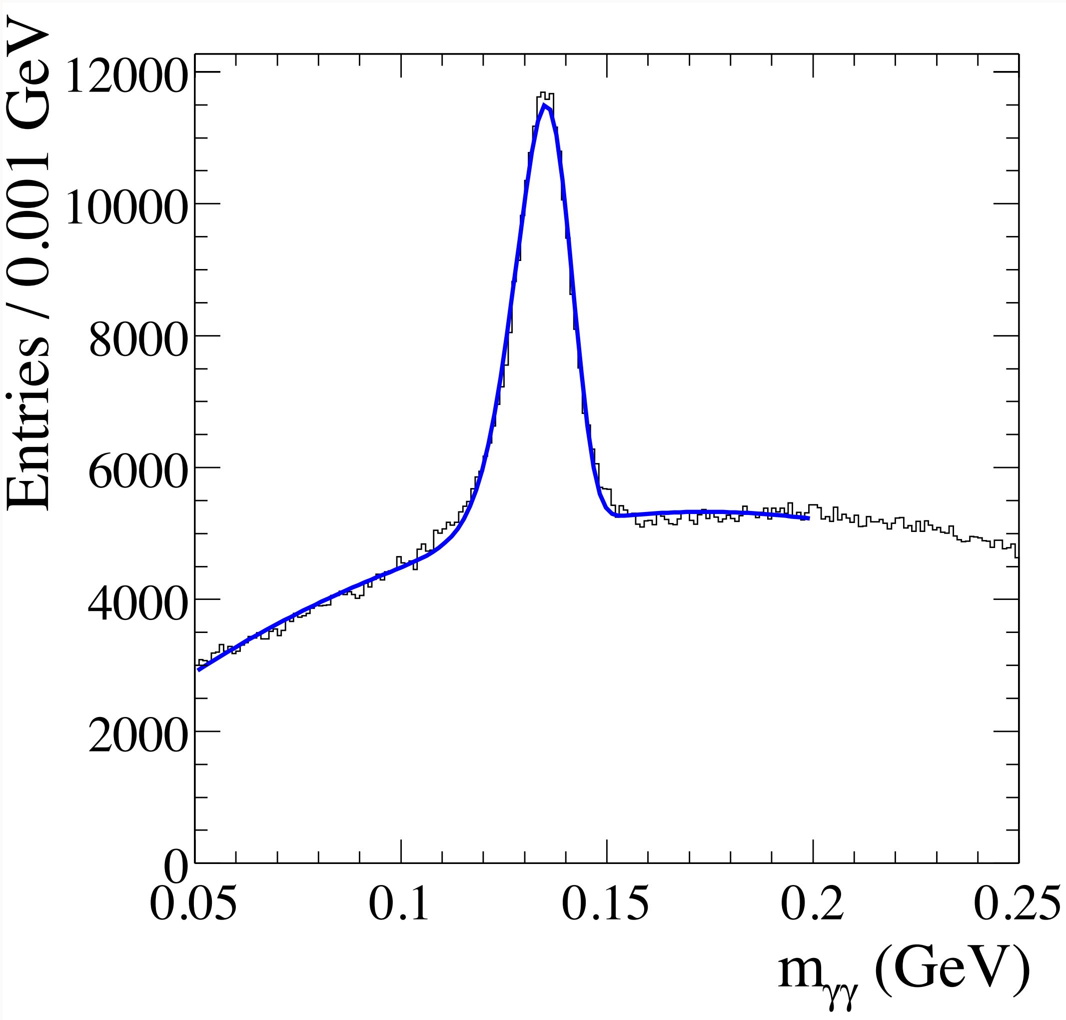

Figure 71. Invariant mass of two photons in $B\overline{B}$ events. The energies of the photons and the π^0 are required to exceed 30 MeV and 300 MeV, respectively. The solid line is a fit to the data.

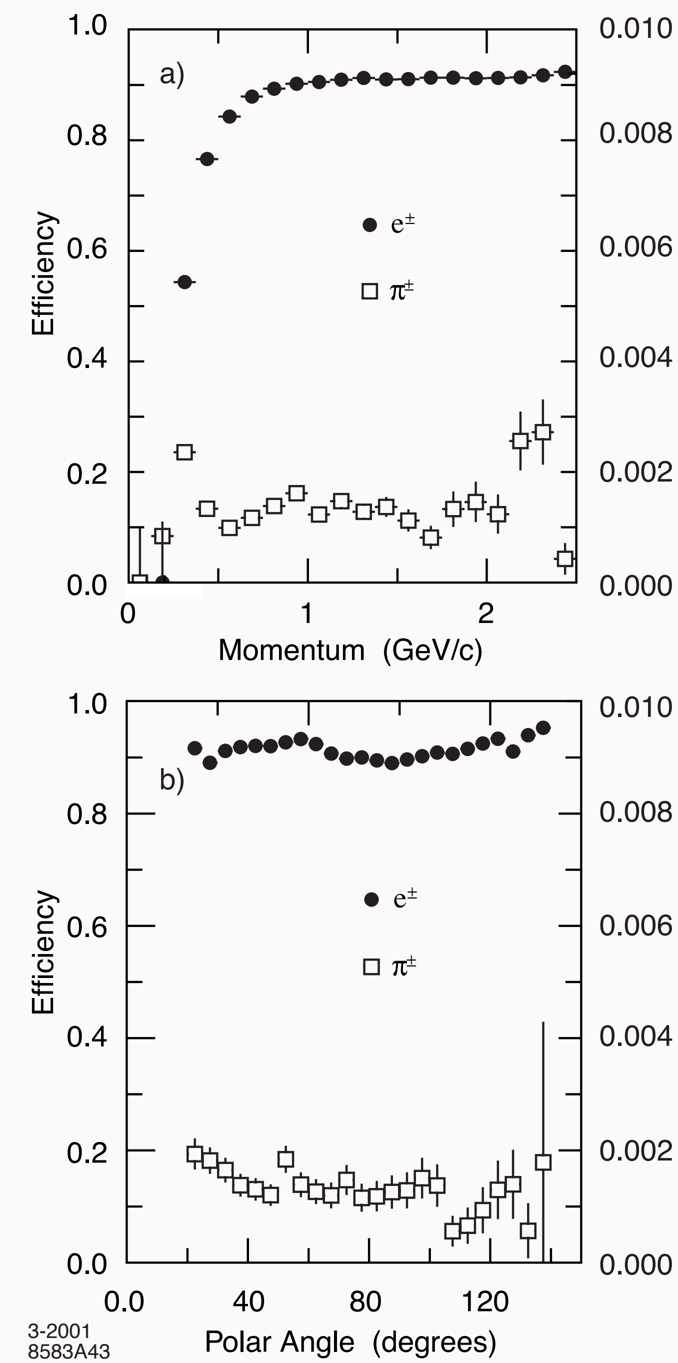

Figure 72. The electron efficiency and pion mis-identification probability as a function of a) the particle momentum and b) the polar angle, measured in the laboratory system.

Instrumented Flux Return

INSTRUMENTED FLUX RETURN V1

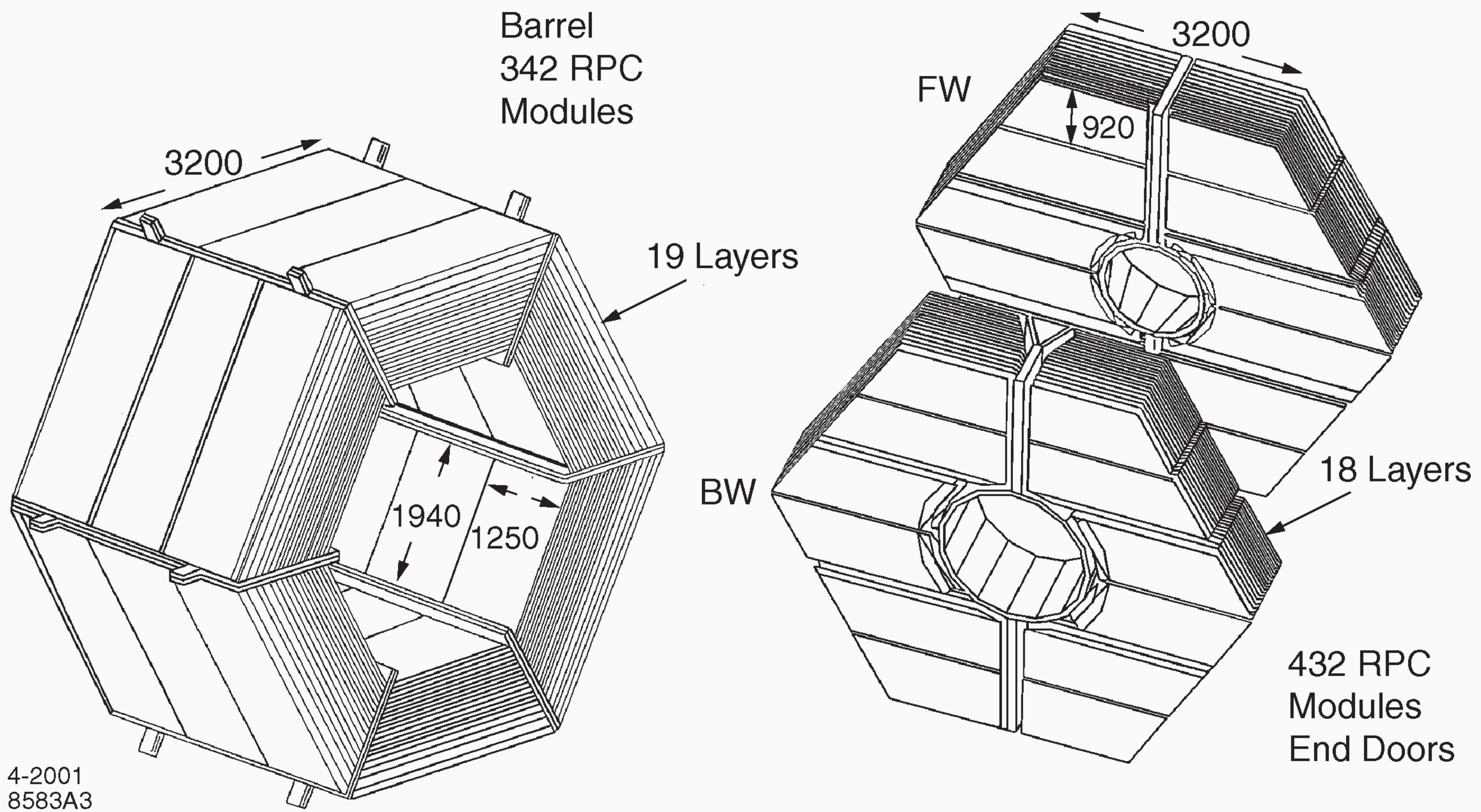

Figure 73. Overview of the IFR: Barrel sectors and forward (FW) and backward (BW) end doors; the shape of the RPC modules and their dimensions are indicated.

Resistive Plate Chambers

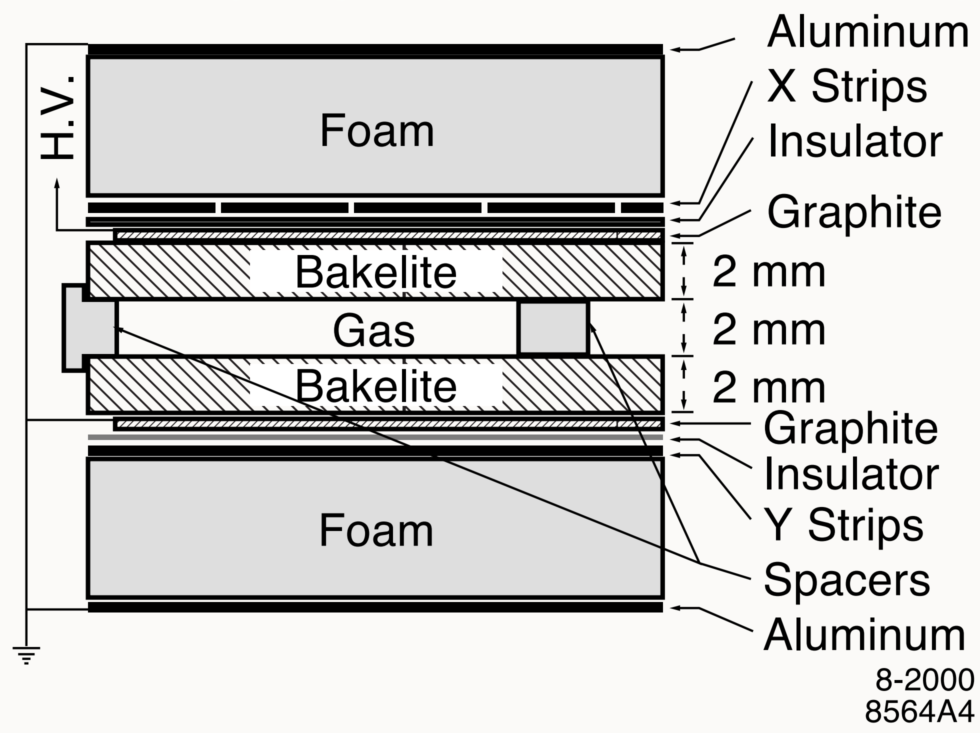

Figure 74. Cross section of a planar RPC with the schematics of the high voltage (HV) connection.

Table 13
IFR Readout segmentation. The total number of channels is close to 53,000.

section	# of sectors	coordinate	# of readout layers	# strips layer/sect	strip length (cm)	strip width (mm)	total # channels
barrel	6	ϕ	19	96	350	19.7-32.8	$\approx 11,000$
		z	19	96	190-318	38.5	$\approx 11,000$
endcap	4	y	18	6x32	124-262	28.3	13,824
		x	18	3x64	10-180	38.0	$\approx 15,000$
cylinder	4	ϕ	1	128	370	16.0	512
		z	1	128	211	29.0	512
		u	1	128	10-422	29.0	512
		v	1	128	10-423	29.0	512

Identificazione dei Muoni

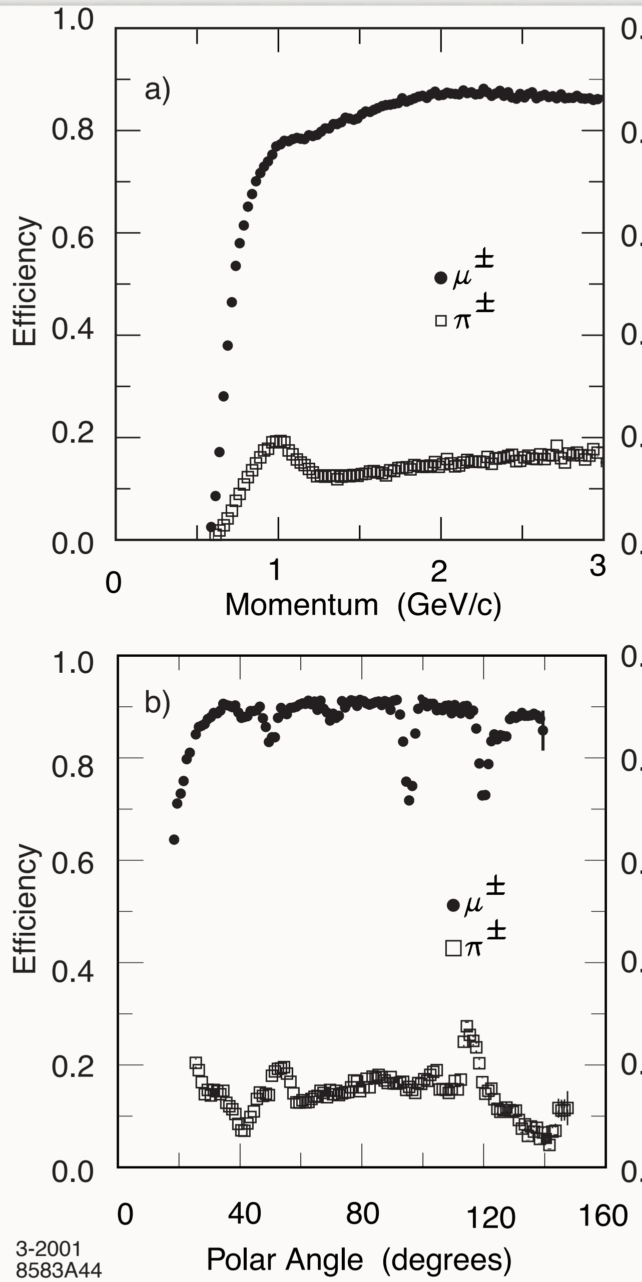

Figure 79. Muon efficiency (left scale) and pion misidentification probability (right scale) as a function of a) the laboratory track momentum, and b) the polar angle (for $1.5 < p < 3.0\,\mathrm{GeV}/c$ momentum), obtained with loose selection criteria.

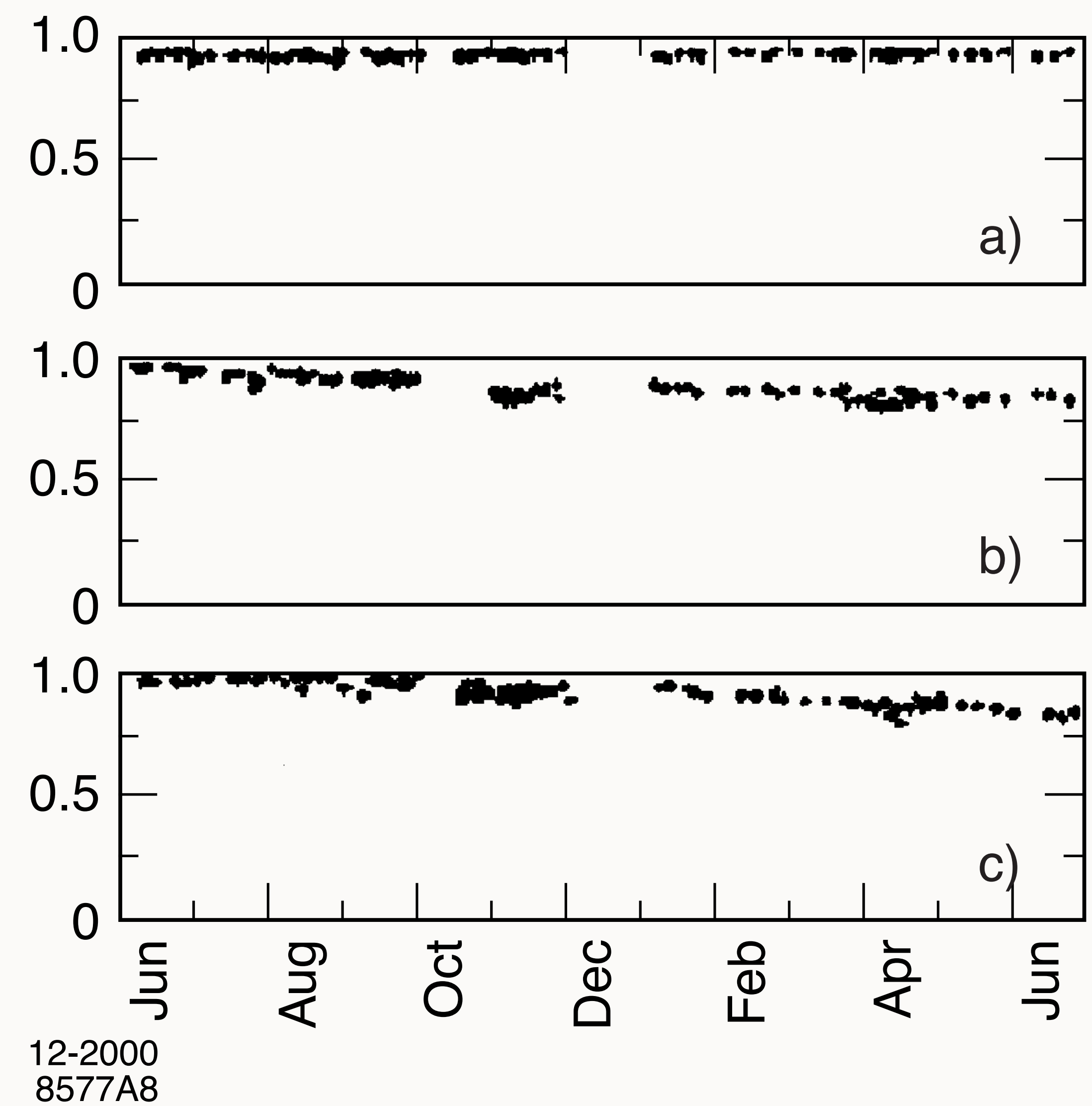

Figure 78. Efficiency history for 12 months starting in June 1999 for RPC modules showing different performance: a) highly efficient and stable; b) continuous slow decrease in efficiency; c) more recent, faster decrease in efficiency.

TRIGGER

Event type	Cross section (nb)	Production Rate (Hz)	Level 1 Trigger Rate (Hz)
$b\bar{b}$	1.1	3.2	3.2
other $q\bar{q}$	3.4	10.2	10.1
e^+e^-	$\sim$53	159	156
$\mu^+\mu^-$	1.2	3.5	3.1
$\tau^+\tau^-$	0.9	2.8	2.4

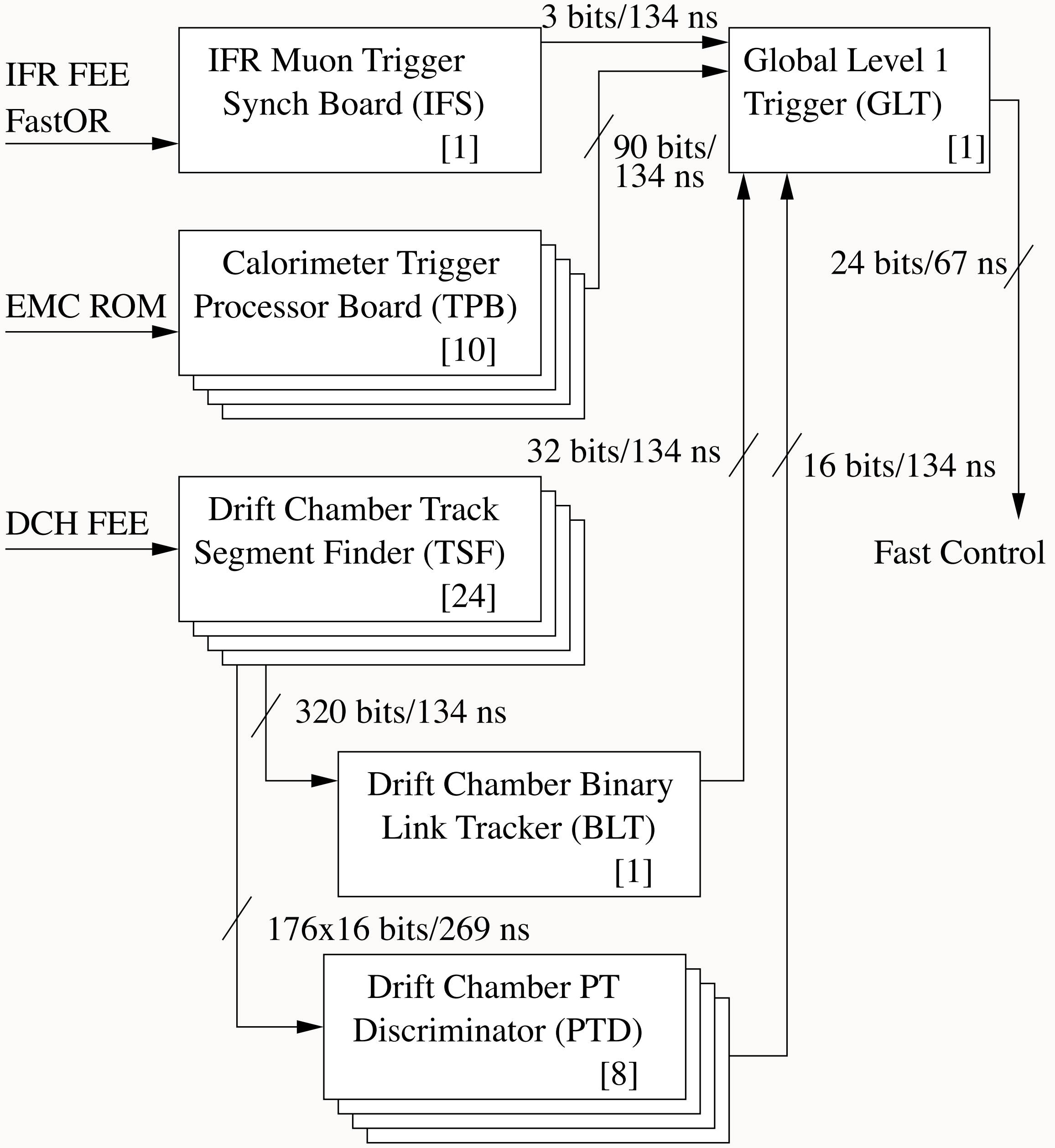

Figure 82. Simplified L1 trigger schematic. Indicated on the figure are the number of components (in square brackets), and the transmission rates between components in terms of total signal bits.

TRIGGER

Table 15
Trigger primitives for the DCT and EMT. Most energy thresholds are adjustable; those listed are typical values.

	Description	Origin	No. of bits	Threshold
B	Short track reaching DCH superlayer 5	BLT	16	120 MeV/c
A	Long track reaching DCH superlayer 10	BLT	16	180 MeV/c
A′	High p_{t} track	PTD	16	800 MeV/c
M	All-θ MIP energy	TPB	20	100 MeV
G	All-θ intermediate energy	TPB	20	250 MeV
E	All-θ high energy	TPB	20	700 MeV
X	Forward endcap MIP	TPB	20	100 MeV
Y	Backward barrel high energy	TPB	10	1 GeV

Table 17
Level 1 Trigger efficiencies (%) and rates (Hz) at a luminosity of $2.2 \times 10^{33}\,\mathrm{cm}^{-2}\mathrm{s}^{-1}$ for selected triggers applied to various physics processes. The symbols refer to the counts for each object.

Level 1 Trigger	$\varepsilon_{B\overline{B}}$	$\varepsilon_{B\to\pi^0\pi^0}$	$\varepsilon_{B\to\tau\overline{\nu}}$	$\varepsilon_{c\overline{c}}$	ε_{uds}	ε_{ee}	$\varepsilon_{\mu\mu}$	$\varepsilon_{\tau\tau}$	Rate
A≥3 & B* ≥1	97.1	66.4	81.8	88.9	81.1	—	—	17.7	180
A≥1 & B* ≥1 & A′ ≥1	95.0	63.0	83.2	89.2	85.2	98.6	99.1	79.9	410
Combined DCT (ORed)	99.1	79.7	92.2	95.3	90.6	98.9	99.1	80.6	560
M≥3 & M* ≥1	99.7	98.6	93.7	98.5	94.7	—	—	53.7	160
EM* ≥1	71.4	94.9	55.5	77.1	79.5	97.8	—	65.8	150
Combined EMT (ORed)	99.8	99.2	95.5	98.8	95.6	99.2	—	77.6	340
B≥3 & A≥2 & M≥2	99.4	81.2	90.3	94.8	87.8	—	—	19.7	170
M* ≥1 & A≥1 & A′ ≥1	95.1	68.8	83.7	90.1	87.0	97.8	95.9	78.2	250
E≥1 & B≥2 & A≥1	72.1	92.4	60.2	77.7	79.2	99.3	—	72.8	140
M* ≥1 & U≥5 (μ-pair)	—	—	—	—	—	—	60.3	—	70
Combined Level 1 triggers	>99.9	99.8	99.7	99.9	98.2	>99.9	99.6	94.5	970